# Second-Order Sliding Mode Control of Wind Turbines to Enhance the Fault-Ride Through Capability Under Unbalanced Grid Faults

K. Tahir[1,2*], T. Allaoui[2], M. Denai[3], S. Mekhilef[4], C. Belfedal[2], M. Doumi[5]

[1]School of Electrical and Energetic Engineering of Oran, Oran, Algeria.
[2]Department of Electrical Engineering, L2GEGI Laboratory, Ibn Khaldoun University, Tiaret, Algeria.
[3]School of Engineering & Computer Science, University of Hertfordshire, Hatfield AL10 9AB, UK
[4]Power Electronics and Renewable Energy Research Laboratory (PEARL), Department of Electrical Engineering, University of Malaya, Kuala Lumpur, Malaysia
[5]Department of Electrical Engineering, CAOSEE Laboratory, Béchar University, Algeria.

[*] tahir.commande@gmail.com

## Abstract

The integration of wind generation to the grid is growing rapidly across the world. As a result, grid operators have introduced the so-called grid codes (GC), which nowadays include a range of technical conditions and requirements, which wind generators must fulfill. Among these, the low voltage ride through (LVRT) is a requirement for wind turbines to stay connected to the grid and continue to operate during the disturbance. In this study, a control structure, combining inertial kinetic energy storage with a crowbar circuit, is proposed to enhance the ride-through capability of a wind turbine generator (WTG) based on a wound-field synchronous generator (WFSG) under unsymmetrical voltage dips. For the grid-side converter (GSC), a decoupled double synchronous reference frame (DDSRF) d-q current controller is used. Furthermore, a Second-Order Sliding Mode Controller (SOSMC) with Super-twisting (ST) algorithm is proposed for the GSC and the machine-side converter (MSC) to improve the response speed and achieve an accurate regulation of the dq-axis current components simultaneously.  The main objectives of the GSC are to achieve a balanced, sinusoidal current and smooth the real and reactive powers to reduce the influence of the negative sequence voltage. A series of simulations are presented to demonstrate the effectiveness of the proposed control scheme in improving the LVRT capability of the WFSG-driven wind turbine and the power quality of the system under unbalanced grid voltage conditions.

**Keywords**: Wind turbine, wound-field synchronous generator, low voltage ride-through, decoupled double synchronous reference frame, Super-twisting algorithm; Second-Order Sliding Mode Controller.

**Nomenclature**

| | | | |
|---|---|---|---|
| $v_s$ , $i_s$ | stator voltage and current | $M_{sD}$ | mutual inductance between the stator and direct damper |
| $v_f$ , $i_f$ | voltage and current of the main field winding | $M_{sQ}$ | mutual inductance between the stator and quadrature damper |
| $i_D$ , $i_Q$ | direct and quadrature damper currents | $\omega_e$ , $\omega_g$ | electrical and grid angular frequencies |
| $r_s$ , $r_f$ , $r_D$ , $r_Q$ | Resistances of the stator, main field and dampers | $\theta_g$ | grid voltage angle |
| $L_d$ , $L_q$ | inductances of the direct and quadrature stator windings | $\Omega_m$ | mechanical generator speed |
| $L_f$ , $L_D$ , $L_Q$ | inductances of the main field, direct and quadrature dampers | $v_g$, $i_g$ | grid-side converter (GSC) output voltage and current |
| $M_{sf}$ | mutual inductance between direct stator winding and main field | $P_s$ , $Q_s$ | stator active and reactive powers |
| $M_{fD}$ | mutual inductance between main field winding and direct damper | $P_g$ , $Q_g$ | GSC active and reactive output powers |

**Acronyms**

| | | | |
|---|---|---|---|
| AFRST | adaptive fuzzy RST controller | PNS | positive and negative sequence |
| B2B | back-to-back converter | PR | proportional-resonant |
| DDSRF | decoupled double synchronous reference frame | PWM | pulse width modulation |
| FRT | fault ride through | ROGI | reduced-order generalized integrator |
| GCC | grid connected converters | ROR | reduced-order resonance |
| GC | Grid code | RST | R-S-T are polynomials |
| GSC | grid side converter | SOGI | second order generalized integrator |
| LPF | low pass filter | SOSMC | Second-Order Sliding Mode Controller |
| LVRT | low-voltage ride-through | ST | Super-twisting algorithm |
| MPPT | maximum power point tracking | WECS | wind energy conversion system |
| MSC | machine side converter | WFSG | wound field synchronous generator |
| NS | negative sequence | WT | wind turbine |
| PI | proportional-integral | | |

**Subscripts**                                                        **Superscripts**

| | | | |
|---|---|---|---|
| $s$, $g$ | stator, GSC | $+$ , $-$ | synchronous positive and negative reference frames |
| $\alpha$ , $\beta$ | stationary axes | $*$ | complex conjugate |
| $d$ , $q$ | synchronous axes | | |
| $+$, $-$ | positive and negative sequence components | | |

## I. INTRODUCTION

Today, wind power is one of the dominant renewable energy sources worldwide and it is projected to increase substantially in the years ahead [1]. The global cumulative installed capacity is projected to reach 840 GW by the end of 2022 [2]. This rapid growth can have a huge impact on the distribution grid, particularly under unbalanced faults [3]. As a result, in many countries with a large share of renewable generation especially wind farms, grid codes (GC) have been revised and enforced by Transmission System and Distribution System Operators (TSOs and DSOs) to enhance the stability and security of power systems. Low-voltage ride-through (LVRT) or fault-ride through (FRT) is a major requirement for the integration of wind generators into the grid [4, 5]. LVRT requires that wind energy conversion systems (WECSs) should stay connected to the grid and must supply reactive power to help restore the grid voltage following a disturbance in the grid [6-8]. Recently, due to the large deployment of distributed renewable energy sources several countries have revised their GCs requirements. In Fig. 1 are depicted the GCs for Germany, Spain, and Denmark. From this chart, it is clear that each country has different minimum voltage values referred to as $V_{fault}$, the time up to which this voltage should be maintained is denoted by $T_{fault}$ and the voltage up to which it should be recovered is denoted by $V_{recovery}$ within the duration of $T_{recovery}$ [9]. For instance, for Germany, according to E.ON-GCs [10] for a $T_{fault} = 150$ ms the $V_{fault}$ is up to 0 pu and has to hit $V_{recovery} = 0.9$ pu within recovery time of $T_{recovery} = 1500$ ms.
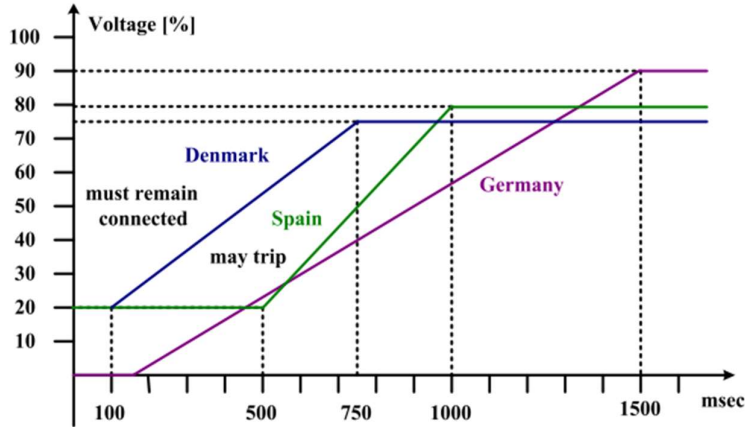


Fig. 1 Fault ride through grid codes for Germany, Spain and Denmark.

In wind power generation, the Doubly-Fed Induction Generator (DFIG)-based wind turbine (WT) has become one of the most favourable choices because it presents many advantages, such as reduced power converter rating (25–30% of the generator nominal power) and low cost [11]. However, because of the relation of its stator right to the grid, this wind turbine design is very prone to grid faults [12]. Unlike the previous design, this paper proposes a wind turbine topology based on a Wound Field Synchronous Generator (WFSG) with a full-scale back-to-back (B2B) pulse width modulated (PWM) converter that provides complete decoupling between the generator and the grid, enhancing its capacity to fulfill the LVRT requirement. On the other hand, the WFSG has high efficiency as it uses the whole stator current to generate the electromagnetic torque, and it directly regulates a power factor [13, 14].

The negative sequence (NS) component appears in the grid voltages when the grid-side converter (GSC) operates under unbalanced conditions, resulting in significant double frequency ripples in the real and reactive powers [15].

Furthermore, the oscillating power causes voltage fluctuations with double frequency in the DC capacitor, which will undermine the smoothing characteristics of the capacitor and reduce its lifetime [16]. Odd harmonics are also generated in the AC grid current, resulting in distortion and unbalance of the input current. Consequently, if no control is applied to the unbalanced voltage in the WFSG, the WT, may have to be isolated from the grid, which is not acceptable according to the new GCs [10, 17]. Therefore, during certain steady-state voltage unbalance condition, the WFSG-based WECSs should operate without tripping.

Various approaches for FRT capacity enhancement of wind turbines have been suggested in the literature. Current methods adopted to enhance the FRT capacity of wind generators are based on external devices. These include braking choppers [18-20], energy storage systems [21, 22], series dynamic braking resistors [23-25], auxiliary parallel grid-side converters [26], and electronic power transformers [27]. The cost of these external devices is high and their implementation is very complex. The authors in [28], suggested a resistive-type Superconducting Fault Current Limiter (SFCL) to improve the efficiency of a Permanent Magnet Synchronous Generator-based WECS linked to a DC micro-grid. However, the PMSG's fault behaviour is distinct from the AC grid-related PMSG behaviour. In [29], the flux-coupling SFCL design is updated and adapted to improve the capability of FRT for the PMSG. A combination of a FRT system of SFCL and ESS was proposed and implemented in [30].

While the use of SFCL in grid-connected PMSG improves the capability of FRT, its resistance value cannot be controlled to adapt to various voltage sag faults. In [31-33], the Bridge-type FCL (BFCL) with the ability to regulate voltage dip for FRT improvement of the DFIG and squirrel cage induction generator was proposed. This device has a variable resistance for a wider range of voltage sags. However, the BFCL switch produces a high voltage spike which may cause problems during the operation. To address this problem in the BFCL circuit, the authors in [34] proposed a Multi-Step Bridge-type Fault Current Limiter (MSBFCL) to ride-through the PMSG under a larger scale of voltage sag faults. Another effective approach uses a series compensation device, for example, a Dynamic Voltage Restorer (DVR) [35], which seeks to regulate the grid voltage and frequency within their rated values during voltage unbalance. However, the DVR may not endure voltage unbalances having a relatively longer duration because of its limited DC-link capacity [36]. However, by improving the control and compensation technique, the DVR can give a better performance. In [9], the authors suggested that the FRT capability of the DFIG-WT could be improved during both symmetrical and asymmetrical grid faults, by applying a synchronous reference frame (SRF) control to the DVR. In [37], the authors proposed a DVR with combined feed-forward and feed-back (CFFFB) control to improve the FRT capability of DFIG-WTs.

More recently, several control strategies have been suggested to overcome these problems such as dual current control [38, 39], direct power control [40], and predictive current control [41, 42]. The positive and negative sequence (PNS) of the current can be regulated simultaneously by the dual current control method. Yet, oscillations have been observed in the d-q signals from the interaction of current vectors with reference frames.

This paper proposes a DDSRF controller approach for decoupling the oscillation counteracts induced by the existence of both sequences [43].

The integrated limiter setting for the PI controller in the overall system is proposed in [44]. Other control methods based on resonant controllers have also been discussed. In [45-47], a PI controller and a resonant controller (PI–R) were designed in the positive synchronous frame to control the NS currents and reduce harmonics. Moreover, both the PNS currents were controlled by the proportional resonant (PR) controller in the stationary reference frame. A conventional PI controller plus a second-order generalized integrator (SOGI) was used to control the PNS current components and achieve zero steady-state error. However, the authors in [46, 48] pointed out that in order to track both components at a fixed frequency, the SOGI is very reliable since it has two poles. This will lead to the injection of the third harmonic current into the grid. In [49-52], the authors proposed a reduced-order generalized integrator (ROGI) instead of the SOGI in the PR regulator, and this control structure was termed a reduced-order resonance (ROR) regulator. This regulator can give accurate control of the NS current in the positive synchronous frame. As a result, this method improves the performance of the grid-connected inverter. However, this proposed controller was sensitive to grid frequency deviations. Because of the nonlinear characteristics of the wind turbine generator and external disturbances, nonlinear and robust controllers such as adaptive fuzzy RST (AFRST) regulator [53], interval type-2 fuzzy logic control (IT-2 FLC) [54], high-order sliding mode (HOSM) controller [55], a modified SMC based model predictive control [56], have been proposed. However, these controllers ensure zero steady-state error only for the positive sequence component of the grid current, but not the NS component. This limitation is undesirable under unbalanced grid conditions.

This paper aims to enhance the LVRT capability and improve the transient stability of wind generator systems during grid faults. The major contributions of this paper are summarized in the following points:

1. A ST algorithm with SOSMC is designed to achieve a robust and fast current control for the WFSG-based WECS.

2. The proposed approach is based on storing excess energy in the turbine generator's inertia during LVRT, meanwhile, when the wind turbine exceeds the maximum rotor speed during a fault, a crowbar circuit is used to avoid system instability.

3. Implementation of a DDSRF d-q current controller in the GSC.

4. Three control techniques are designed for the GSC to minimize the NS voltage effect on the WFSG wind power system performance. They aim to achieve: (i) a balanced and sinusoidal current, (ii) smooth real power and (iii) a smooth reactive power.

The paper is structured as follows. Section 2 presents the model of the WFSG-based wind turbine. The coordinated control of the MSC and GSC is described in Section 3. Section 4 focuses on the application of the LVRT requirement for the limitation of the current of the GSC during the fault. Section 5 describes the design of the ST algorithm with SOSMC for the MSC and GSC in the SRF. Section 6 presents the simulation results and discussions and finally, the conclusions of this contribution are summarised in Section 7.

## II. MODELING OF THE WFSG-BASED WIND ENERGY SYSTEM UNDER UNBALANCED GRID VOLTAGE

Fig. 2 depicts a block diagram of the WECS used in this simulation study, which consists of a WFSG, a B2B two-level converter. The B2B converter is composed of the MSC and GSC, which are linked through the DC bus. The system is also fitted with a crowbar circuit for stable operation under grid fault.

The supervisory control system monitors the grid voltage amplitude, phase angle, and frequency. In the event of grid faults, appropriate control signals are sent to adjust the references for the controlled variables. During both

normal and LVRT operation, the reference generation block calculates the references for $dq$-axis stator currents for the MSC, while the reference $dq$-axis grid currents are developed for the GSC [4].

The control objectives for the B2B converter are as follows:

- For the MSC:
  a) Regulation of the $q$-axis stator current to maximize the power of the turbine generator during normal operation and to store the excess of real power in the inertia during LVRT operation.
  b) Control of the $d$-axis stator current to obtain the stator reactive power.
- For the GSC:
  a) Maintain the DC-link voltage at the required level and limit the real power injected into the grid with the $d$-axis grid current controller during normal and LVRT operations respectively.
  b) Regulate the reactive power injected into the grid via the $q$-axis grid current.
  c) Grid synchronization.

The NS components under the balanced condition of the voltages and currents are considered in the model. Detailed modeling of the MSC and GSC is presented in the subsequent sections.
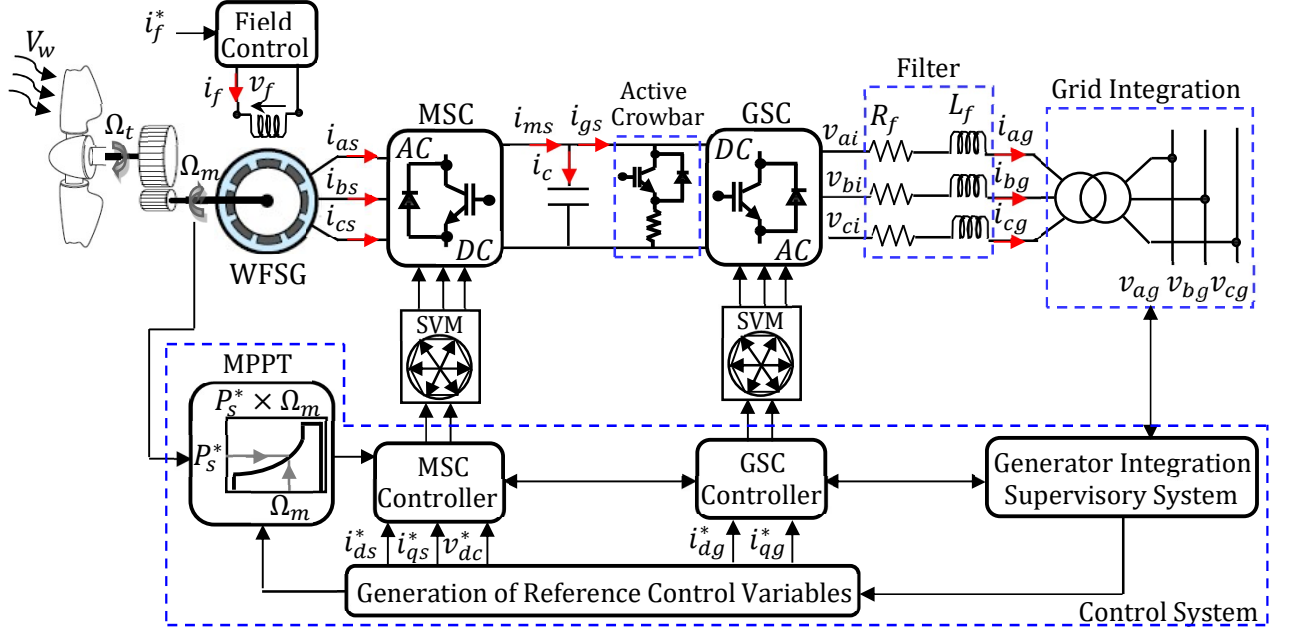


Fig. 2 Configuration of the WECS wind turbine system and its control scheme.

**A. Modeling of the WFSG**

The WFSG voltage equations in the synchronous $d$-$q$ reference frame are expressed as [57]:

$$\begin{cases} v_{ds} = -r_s i_{ds} + \omega_e L_{qs} i_{qs} - \omega_e M_{sQ} i_Q - L_{ds} \dfrac{di_{ds}}{dt} + M_{sf} \dfrac{di_f}{dt} + M_{sD} \dfrac{di_D}{dt} \\[2mm] v_{qs} = -r_s i_{qs} - \omega_e L_{ds} i_{ds} + \omega_e M_{sf} i_f + \omega_e M_{sD} i_D - L_q \dfrac{di_{qs}}{dt} + M_{sQ} \dfrac{di_Q}{dt} \\[2mm] v_f = r_f i_f + L_f \dfrac{di_f}{dt} - M_{sf} \dfrac{di_{ds}}{dt} + M_{fD} \dfrac{di_D}{dt} \\[2mm] 0 = r_D i_D + M_{fD} \dfrac{di_f}{dt} - M_{sD} \dfrac{di_{ds}}{dt} + L_D \dfrac{di_D}{dt} \\[2mm] 0 = r_Q i_Q - M_{sQ} \dfrac{di_{qs}}{dt} + L_Q \dfrac{di_Q}{dt} \end{cases} \tag{1}$$

The electrical angular speed $\omega_e$ of the WFSG is given by:

$$\omega_e = p\, \Omega_m \tag{2}$$

The electromagnetic torque is given by:

$$T_{em} = p\big(\phi_{ds} i_{qs} - \phi_{qs} i_{ds}\big)$$

$$= p\big[(L_q - L_d) i_{ds} i_{qs} + (M_{sf} i_f + M_{sD} i_D) i_{qs} - M_{sQ} i_Q i_{ds}\big] \tag{3}$$

And the real and reactive powers are given as:

$$\begin{cases} P_s = v_{ds} i_{ds} + v_{qs} i_{qs} \\ Q_s = v_{qs} i_{ds} - v_{ds} i_{qs} \end{cases} \tag{4}$$

**B. Modeling of the GSC**

Under an unbalanced supply, the GSC behaves like a grid-connected voltage source converter. Under the assumption that there is no zero-sequence component and the network is unbalanced, then GSC can be separated into a PNS. Thus, the state-space model of the GSC in the positive and negative SRFs can be written as:

$$\frac{d}{dt}\begin{bmatrix} i_{dg}^+ \\ i_{qg}^+ \end{bmatrix} = A \begin{bmatrix} i_{dg}^+ \\ i_{qg}^+ \end{bmatrix} + B_i \begin{bmatrix} v_{di}^+ \\ v_{qi}^+ \end{bmatrix} + B_g \begin{bmatrix} v_{dg}^+ \\ v_{qg}^+ \end{bmatrix} \tag{5}$$

$$\frac{d}{dt}\begin{bmatrix} i_{dg}^- \\ i_{qg}^- \end{bmatrix} = A^{-1} \begin{bmatrix} i_{dg}^- \\ i_{qg}^- \end{bmatrix} + B_i \begin{bmatrix} v_{di}^- \\ v_{qi}^- \end{bmatrix} + B_g \begin{bmatrix} v_{dg}^- \\ v_{qg}^- \end{bmatrix} \tag{6}$$

With

$$A = \begin{bmatrix} -\dfrac{R_f}{L_f} & \omega_g \\[3mm] -\omega_g & -\dfrac{R_f}{L_f} \end{bmatrix} \quad ; \quad B_i = \begin{bmatrix} \dfrac{1}{L_f} & 0 \\[3mm] 0 & \dfrac{1}{L_f} \end{bmatrix} \quad ; \quad B_g = \begin{bmatrix} -\dfrac{1}{L_f} & 0 \\[3mm] 0 & -\dfrac{1}{L_f} \end{bmatrix}$$

Where $R_f$ and $L_f$ represent the grid filter resistance and inductance respectively; the superscripts "+" and "−" denote the PNS components respectively; $i_{dg}, i_{qg}$ are the $dq$ grid currents; $v_{dg}, v_{qg}$ are the $dq$ grid voltages; $v_{di}, v_{qi}$ are the $dq$ voltages generated at the inverter terminals.

The PNS components of the apparent power which have been delivered to the grid under unbalanced conditions are given below:

$$S_g = \frac{3}{2}\left\{ \big(e^{j\omega t} v_{dqg}^+ + e^{-j\omega t} v_{dqg}^-\big) \times \big(e^{j\omega t} i_{dqg}^+ + e^{-j\omega t} i_{dqg}^-\big)^* \right\} \tag{7}$$

The superscript "*" denotes the complex conjugate operator.

Thus, from $S_g = P_g + jQ_g$, the instantaneous real ($P_g$) and reactive ($Q_g$) powers are expressed as [43] :

$$P_g = P_0 + P_{c2}\cos(2\omega t) + P_{s2}\sin(2\omega t) \tag{8}$$

$$Q_g = Q_0 + Q_{c2}\cos(2\omega t) + Q_{s2}\sin(2\omega t) \tag{9}$$

Where $P_0$ and $Q_0$ are the average components of the grid real and reactive powers, $P_{c2}, Q_{c2}$ and $P_{s2}, Q_{s2}$ are the oscillating components of the real and reactive powers at twice the grid frequency.

Writing the power terms of equations (8) and (9) in matrix form gives:

$$\begin{bmatrix} P_0 \\ Q_0 \\ P_{c2} \\ P_{s2} \\ Q_{c2} \\ Q_{s2} \end{bmatrix} = \frac{3}{2}\begin{bmatrix} v_{dg}^+ & v_{qg}^+ & v_{dg}^- & v_{qg}^- \\ v_{qg}^+ & -v_{dg}^+ & v_{qg}^- & -v_{dg}^- \\ v_{dg}^- & v_{qg}^- & v_{dg}^+ & v_{qg}^+ \\ v_{qg}^- & -v_{dg}^- & -v_{qg}^+ & v_{dg}^+ \\ v_{qg}^- & -v_{dg}^- & v_{qg}^+ & -v_{dg}^+ \\ -v_{dg}^- & -v_{qg}^- & v_{dg}^+ & v_{qg}^+ \end{bmatrix}\begin{bmatrix} i_{dg}^+ \\ i_{qg}^+ \\ i_{dg}^- \\ i_{qg}^- \end{bmatrix} \tag{10}$$

Finally, the equation of the DC-link voltage is expressed as:

$$C\frac{dv_{dc}}{dt}.v_{dc} = P_s - P_g \tag{11}$$

## III. CONTROL SYSTEM OF MSC AND GSC

### A. MSC control

To meet the LVRT requirements, the real power injected into the grid must be zero ($P_g = 0$) during grid voltage sags. If no specific control is applied to the MSC during a voltage dip, then the real power from the generator can be greater than that delivered to the grid. This can cause an over-voltage on the DC-link and damage the capacitor or the power converter [4, 14]. With the proposed control strategy, the generator speed is increased through proper control of the MSC by reducing the generator power to zero during the fault, to absorb and convert the incoming wind energy into kinetic energy and store it in the wind turbine inertia. After fault clearance, this kinetic energy is converted back to electric energy and re-injected into the grid. To describe the principle of inertial kinetic energy storage, the wind turbine should be operated in the partial load region. Under normal operation, the optimal power of the turbine is selected, which corresponds to the optimal rotational speed $\Omega_{m_{opt}}$. Therefore, the storage of the kinetic energy is achieved by a displacement of the operating point so that the turbine rotational speed increases to a higher value $\Omega_{m_2}$ but within the range of rated value [58], as shown in Fig. 3. This causes the efficiency of the wind turbine to decrease and hence the turbine is de-loaded.
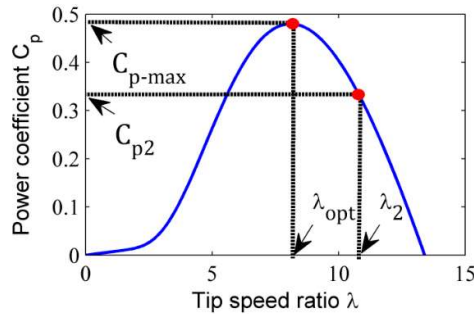


Fig. 3 Displacement of the operating point following inertial kinetic energy storage.

The energy stored in the wind turbine is expressed as:

$$E_{ks} = \int_0^t P_m dt = \frac{1}{2} J \left( \Omega_{m\_2}^2 - \Omega_{m\_opt}^2 \right) \tag{12}$$

Where $P_m$ denotes the mechanical input power to the generator. In the occurrence of a voltage dip, the required additional power to be injected into the grid can be obtained only if the stored kinetic energy is controlled through the acceleration/deceleration of the wind turbine.

$$P_t(\Omega_m) = P_G(\Omega_m) - P_{inj}(\Omega_m) + P_{Losses} \tag{13}$$
$$\text{with } -P_{inj}(\Omega_m) = J \, \Omega_m \frac{d\Omega_m}{dt}$$

The relation between the maximum mechanical rotor speed $\Omega_{m_2}$ and fault duration $(dt = t_f)$ can be derived from (12) as follows:

$$\Omega_{m\_2} = \sqrt{\frac{2P_m t_f}{J} + \Omega_{m\_opt}^2} \tag{14}$$

From equation (14), it can be noted that three factors affect the limit of this control namely fault duration, inertia, over-speed. Concerning the inertia, the generator's over-speed percentage increase is higher in the case of reduced inertia constant than in the case of a larger one. Similarly, it increases for long fault durations.

Most wind turbines have automatic governing systems to protect them against over speeding. As reported in [4], the Mega Volt Permanent Magnet Multipole Synchronous Generator (Yaskawa® Enewin Generator) for wind turbines with sizes from 2 MW to 5 MW at 3000V have the capability to operate at over-speed of 130% for a period of 2 minutes.

In addition, in this paper, protection based on a crowbar circuit is triggered when the wind turbine hits the maximum rotor speed. In that case, the MPPT control is applied again and the extra power produced is dissipated in the crowbar circuit to avoid continuous charge and discharge of the DC-link capacitor.

As mentioned above and according to the national GCs in [4], the wind turbine is able to keep operating for the maximum grid fault duration of 625 ms, and it is permitted to disconnect it afterward.

The control scheme of the MSC against grid faults is depicted in Fig. 4 where $K_p = \frac{1}{p}\left( M_{sf} i_f + M_{sD} i_D \right)$. During a grid fault, the MPPT is deactivated and the DC-link voltage is controlled by the MSC.
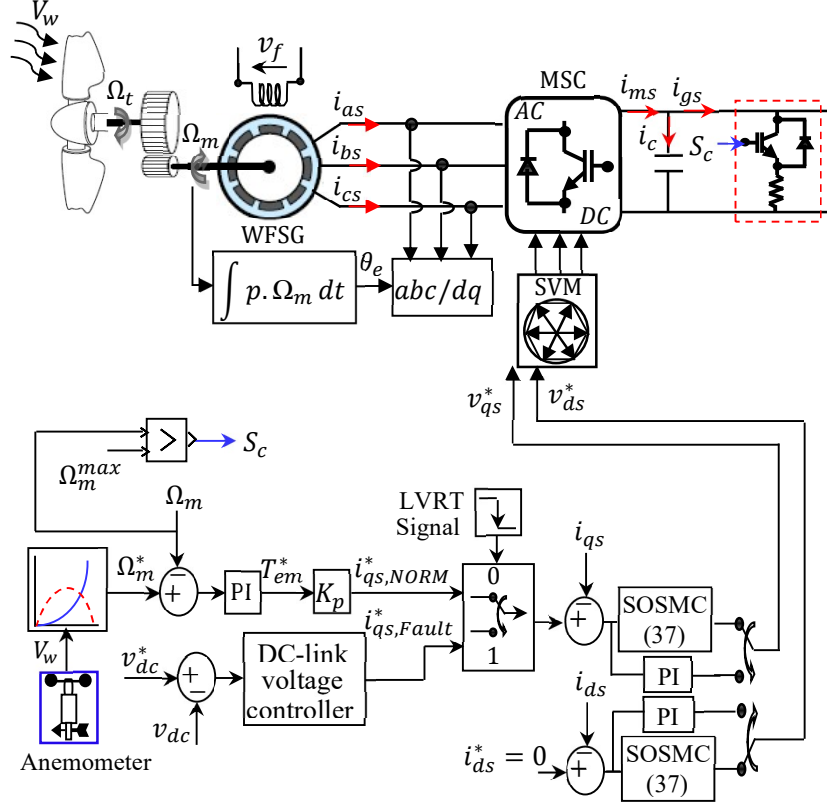
**Fig. 4.** Block diagram of the MSC control scheme against grid fault.

## B. GSC control strategy

According to equation (10), four signals are used in GSC i.e. $i_{dg}^+, i_{qg}^+, i_{dg}^-$ and $i_{qg}^-$ . These signals are controllable and can be used to improve the GSC performance during a fault condition. In order to control the real $P_0$ and reactive power $Q_0$ given in (10), the control of the NS grid current and another two power oscillating terms must be ensured. For this purpose, the following three control targets should be implemented to achieve reliable and stable operation of the power grid and WFSG system. In order to achieve Target (**i**), and to ensure balanced and sinusoidal grid current and less harmonic losses in the three-phase grid, the negative-sequence current should be injected into the grid which will also improve the power quality of the grid.

$$i_{dg}^- = i_{qg}^- = 0 \tag{15}$$

Hence, according to (10) and (15), the PNS reference currents for the GSC are given as:

$$
\begin{cases}
i_{dg}^{+\,*} = \dfrac{2}{3}\left[\dfrac{v_{dg}^+ P_g^* + v_{qg}^+ Q_g^*}{\left(v_{dg}^+\right)^2 + \left(v_{qg}^+\right)^2}\right] \\[2ex]
i_{qg}^{+\,*} = \dfrac{2}{3}\dfrac{P_g^*}{v_{qg}^+} - \dfrac{v_{dg}^+}{v_{qg}^+}\, i_{dg}^{+\,*} \\[2ex]
i_{dg}^{-\,*} = 0 \\[1ex]
i_{qg}^{-\,*} = 0
\end{cases}
\tag{16}
$$

10

The oscillating terms in (8) should be zero with GSC control in order to achieve Target (**ii**), and to ensure smooth real power injection into the power grid which is beneficial for a safe and reliable grid operation, i.e.

$$P_{c2} = P_{s2} = 0 \qquad (17)$$

Then, according to (10) and (17), and applying voltage-oriented control (VOC) theory to GSC, i.e., $v_{qg}^+ = 0$, the reference values of the GSC current components can be calculated as follows:

$$\begin{bmatrix} i_{dg}^{+ *} \\ i_{qg}^{+ *} \\ i_{dg}^{- *} \\ i_{qg}^{- *} \end{bmatrix} = \frac{2}{3} \begin{bmatrix} v_{dg}^+ & v_{qg}^+ & v_{dg}^- & v_{qg}^- \\ v_{qg}^+ & -v_{dg}^+ & v_{qg}^- & -v_{dg}^- \\ v_{dg}^- & v_{qg}^- & v_{dg}^+ & v_{qg}^+ \\ v_{qg}^- & -v_{dg}^- & -v_{qg}^+ & v_{dg}^+ \end{bmatrix}^{-1} \begin{bmatrix} P_g^* \\ Q_g^* \\ P_{c2} = 0 \\ P_{s2} = 0 \end{bmatrix} = \frac{2P_g^*}{3K_1} \begin{bmatrix} -v_{dg}^+ \\ -v_{qg}^+ \\ v_{dg}^- \\ v_{qg}^- \end{bmatrix} + \frac{2Q_g^*}{3K_2} \begin{bmatrix} v_{qg}^+ \\ -v_{dg}^+ \\ v_{qg}^- \\ -v_{dg}^- \end{bmatrix} \qquad (18)$$

Where

$$K_1 = \left[ -\left(v_{dg}^+\right)^2 - \left(v_{qg}^+\right)^2 + \left(v_{dg}^-\right)^2 + \left(v_{qg}^-\right)^2 \right]$$

$$K_2 = \left[ \left(v_{dg}^+\right)^2 + \left(v_{qg}^+\right)^2 + \left(v_{dg}^-\right)^2 + \left(v_{qg}^-\right)^2 \right]$$

Similarly, the oscillating terms in (9) should be nullified in order to address Target (**iii**), and smooth the reactive power injected into the power grid, i.e.

$$Q_{c2} = Q_{s2} = 0 \qquad (19)$$

Therefore, the references for the PNS currents for GSC can be calculated from (10) and (19) with $P_g^*$ and $Q_g^*$ obtained from GCs or the grid operator.

$$\begin{bmatrix} i_{dg}^{+ *} \\ i_{qg}^{+ *} \\ i_{dg}^{- *} \\ i_{qg}^{- *} \end{bmatrix} = \frac{2}{3} \begin{bmatrix} v_{dg}^+ & v_{qg}^+ & v_{dg}^- & v_{qg}^- \\ v_{qg}^+ & -v_{dg}^+ & v_{qg}^- & -v_{dg}^- \\ v_{qg}^- & -v_{dg}^- & v_{qg}^+ & -v_{dg}^+ \\ -v_{dg}^- & -v_{qg}^- & v_{dg}^+ & v_{qg}^+ \end{bmatrix}^{-1} \begin{bmatrix} P_g^* \\ Q_g^* \\ Q_{c2} = 0 \\ Q_{s2} = 0 \end{bmatrix} = \frac{2P_g^*}{3K_2} \begin{bmatrix} v_{dg}^+ \\ v_{qg}^+ \\ v_{dg}^- \\ v_{qg}^- \end{bmatrix} + \frac{2Q_g^*}{3K_1} \begin{bmatrix} -v_{qg}^+ \\ v_{dg}^+ \\ v_{qg}^- \\ -v_{dg}^- \end{bmatrix} \qquad (20)$$

## IV. ANALYSIS OF THE LIMITATION OF GSC CURRENT USING LVRT REQUIREMENT DURING UNBALANCED GRID FAULT

During an unbalanced fault condition, the WECS should take full advantage of the GSC capability and overcome its limitation according to the LVRT requirement. On the other hand, because of the excessively high grid current of the GSC under unbalanced grid fault [59], the references for the real power and the injected reactive power into the grid should also be limited as given in Equation (21):

$$\begin{cases} \begin{cases} P_g^* = P_{pr} \\ Q_g^* = 0 \end{cases} & if \quad 0.9V_n \leq V_g \leq V_n \\ \begin{cases} P_g^* = \sqrt{P_{max}^2 - Q_g^{*2}} \\ Q_g^* = 2\left(1 - \frac{V_g}{V_n}\right) P_{pr} \end{cases} & if \quad 0.5V_n \leq V_g < 0.9V_n \\ \begin{cases} P_g^* = 0 \\ Q_g^* = P_{pr} \end{cases} & if \quad 0 \leq V_g \leq 0.5V_n \end{cases} \qquad (21)$$

With

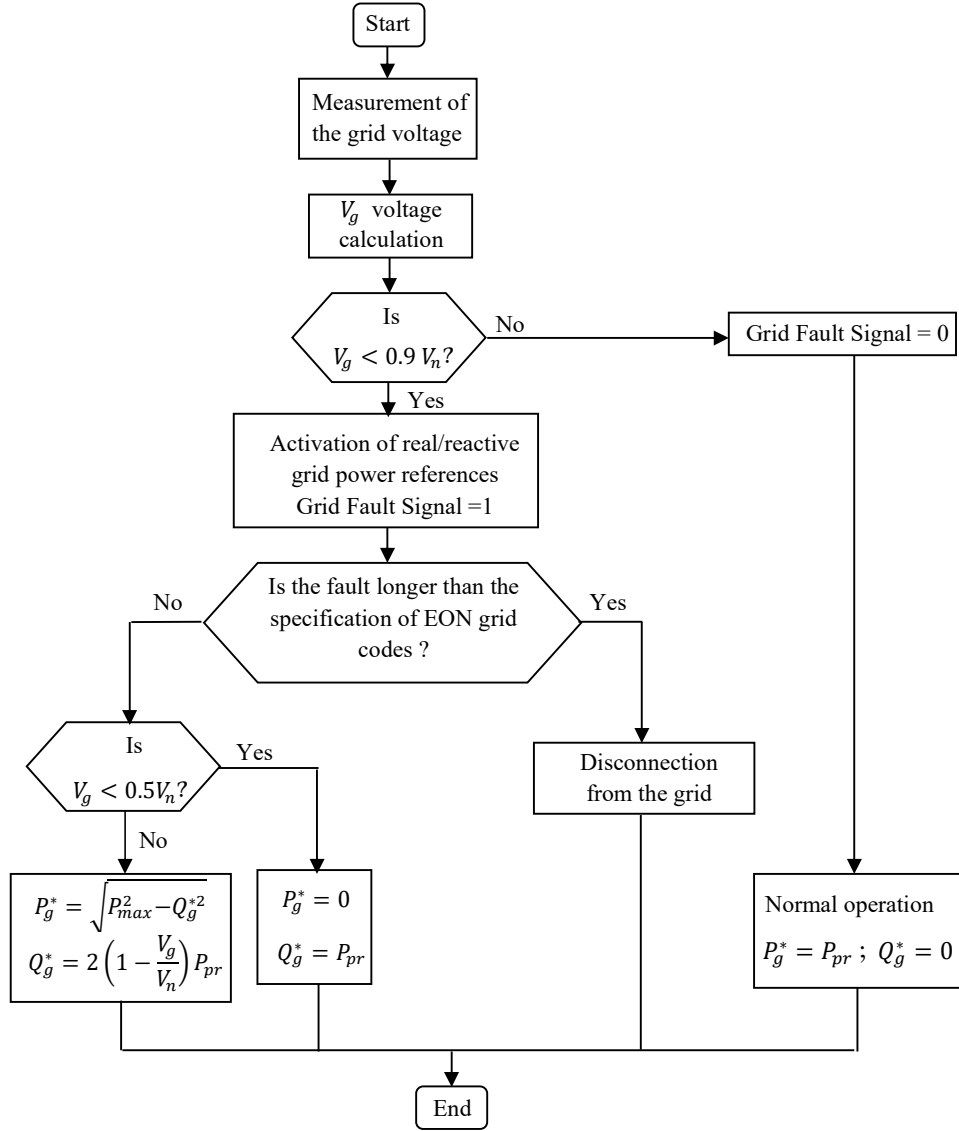$$V_g = \sqrt{\left|v_{dq}^+\right|^2 + \left|v_{dq}^-\right|^2}$$

11

Fig. 5 Flowchart of the LVRT algorithm.

Where $V_n$ and $V_g$ are, respectively, nominal and actual grid voltage, $P_{pr}$ is the output real power before a fault occurring in the grid.

The flowchart of Fig. 5 explains the algorithm used for the LVRT control scheme and the reactive power needed to inject it into the utility grid based on the German GC.

The schematic diagram under asymmetrical voltage dips is shown in Fig. 6. The current loop references can be calculated from equations (16), (18), and (20) in order to achieve Targets (**i**), (**ii**) and (**iii**) respectively.
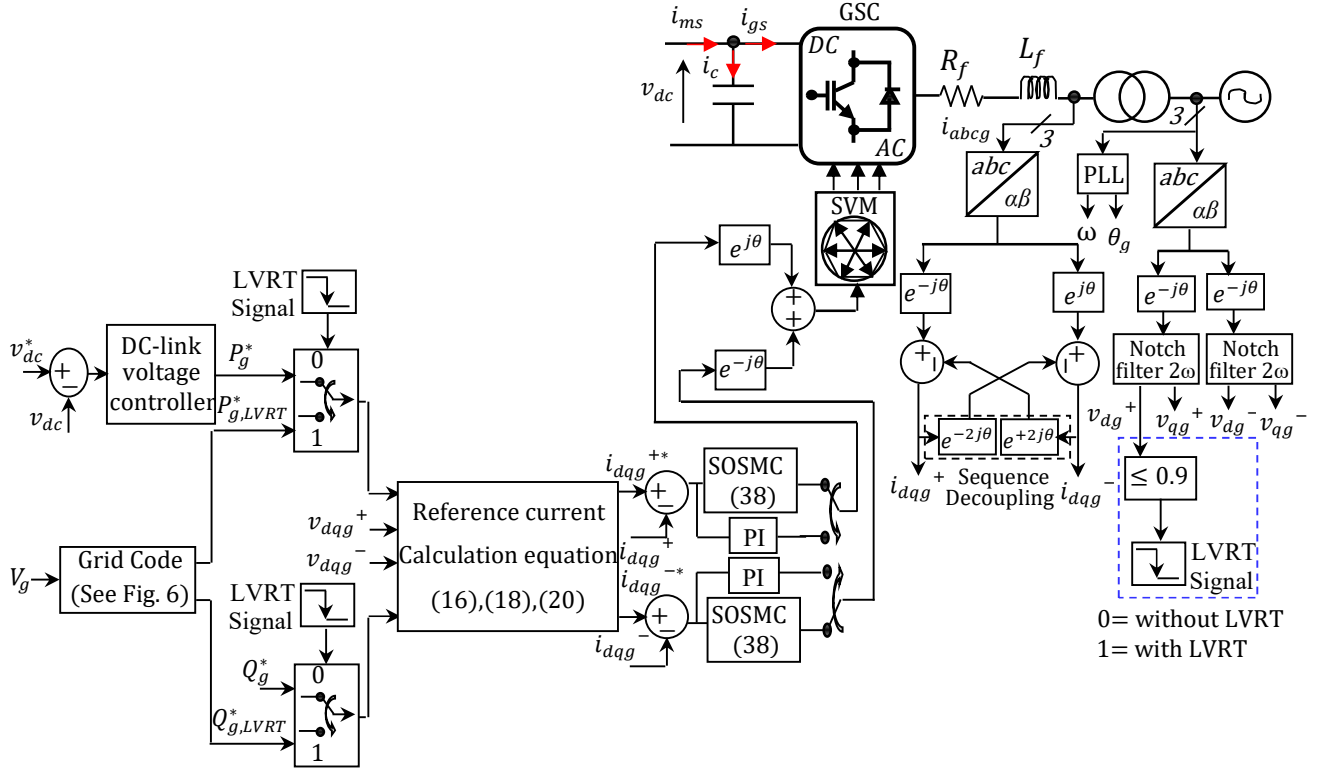
Fig. 6. The control scheme of the GSC under unbalanced grid fault.

## V. CURRENT CONTROLLER DESIGN

Under asymmetrical grid-fault conditions, a dual PI current controller is typically employed to provide the desired system response. However, the time-delay and control errors introduced by the process of extracting both the PNS components using some properly designed filters, such as the notch filter, this may lead to poor system performance and stability. To overcome the problems highlighted above, and in order to remove the 100 Hz oscillation components, a sequence of decoupling algorithms is used [60-62]. Furthermore, the performance of the PI controller is affected, and it requires parameter tuning in order to effectively track the reference value. Thus, a more effective current controller must be designed to achieve the desired response characteristics. A super-twisting algorithm (ST) second-order sliding mode controller (SOSMC) is proposed for both MSC and GSC.

### A. SOSMC Design

Consider the nonlinear single-input single-output system, described in a state-space form as:

$$\dot{x} = f(x) + g(x)v + \xi \tag{22}$$

Where $x$ is the state variable, $v$ is the control input, $\xi$ is the disturbance. $f$ and $g$ are nonlinear functions.

The control objective is to force the sliding variable and its derivative to zero in a finite time which can be written as:

$$s = \dot{s} = 0 \tag{23}$$

Then

$$\dot{s} = f(x) + g(x)v - \dot{x}^* + \xi = u + \xi \tag{24}$$

where $s = x - x^*$, $x^*$ is the reference, and $u$ is a new control input.

In this work, a steady-state tracking error is obtained by applying the SOSM control law for the new control law. One of the key problems with implementing high order sliding mode algorithms is that the number of information required increases with the order of the sliding regime. For example, if a third-order controller is used, then it needs the knowledge of $s, \dot{s}, \ddot{s}$.

Different SOSMC algorithms have been proposed in the literature such as Sub-Optimal (SO), Twisting (TW) and Super Twisting (ST) [63].

In this work, the ST algorithm has been used, as it can be applied directly to the relative degree 1 system. In addition, it only needs s as input information for its implementation. The convergence of this algorithm is also governed by the rotations around the origin of the phase diagram.

The control law u(t) of ST consists of two terms: The first ($u_1$), is defined by its derivative with respect to time while the second ($u_2$), is given by the continuous function of the sliding variable.

The ST control law is defined by:

$$u = u_1 + u_2 \tag{25}$$

With

$$\begin{cases} \dot{u}_1 = -\beta \ sign(s) \\ u_2 = -\alpha \ |s|^{\frac{1}{2}} sign(s) \end{cases} \tag{26}$$

Where $\alpha$ and $\beta$ are positive constants.

Finally, the control input $v^*$ is defined using (24) and (26) as follows:

$$\begin{cases} v^* = \dfrac{1}{g(x)}\left(-f(x) + \dot{x}^* - \alpha \ |s|^{\frac{1}{2}} sign(s) + u_1\right) \\ \dot{u}_1 = -\beta \ sign(s) \end{cases} \tag{27}$$

Substituting (27) into (24), gives

$$\begin{cases} \dot{s} = -\alpha \ |s|^{\frac{1}{2}} sign(s) + u_1 + \xi \\ \dot{u}_1 = -\beta \ sign(s) \end{cases} \tag{28}$$

The candidate Lyapunov function used for the stability analysis of the control system is defined as:

$$V = 2\beta|s| + \frac{1}{2}u_1^2 + \frac{1}{2}\left(-\alpha|s|^{\frac{1}{2}}sign(s) + u_1\right)^2 \tag{29}$$

The Lyapunov form expressed in equation (29) can be defined in a quadratic form by $V = \zeta^T P \ \zeta$, where

$$\zeta^T = \begin{bmatrix} |s|^{\frac{1}{2}}sign(s) & u_1 \end{bmatrix} \quad \text{and} \quad P = \frac{1}{2}\begin{bmatrix} 4\beta + \alpha^2 & -\alpha \\ -\alpha & 2 \end{bmatrix}$$

Its time derivative is expressed as follows

$$\dot{V} = -\frac{1}{|s|^{\frac{1}{2}}}\zeta^T Q_1 \ \zeta + \frac{1}{|s|^{\frac{1}{2}}}\zeta Q_2^T \zeta \tag{30}$$

Where

$$Q_1 = \frac{\alpha}{2}\begin{bmatrix} 2\beta + \alpha^2 & -\alpha \\ -\alpha & 1 \end{bmatrix} \quad \text{and} \quad Q_2^T = \begin{bmatrix} \left(2\beta + \frac{\alpha^2}{2}\right) & -\frac{\alpha}{2} \end{bmatrix}$$

In this analysis, the disturbance $\xi$ is assumed to be unknown but limited and subject to the valued rated current of the inverter($|\xi| \leq \delta I_{max}$), and it can be demonstrated according to [64]

$$\dot{V} \leq -\frac{1}{|s|^{\frac{1}{2}}} \zeta^T Q_3 \, \zeta \tag{31}$$

Where

$$Q_3 = \frac{\alpha}{2}\begin{bmatrix} 2\beta + \alpha^2 - \left(4\frac{\beta}{\alpha} + \alpha\right) & -(\alpha + 2\delta) \\ -(\alpha + 2\delta) & 1 \end{bmatrix}$$

Consequently, $Q_3 \geq 0$ helps to ensure that $\dot{V}$ is negative, which is true if the control parameters $(\alpha, \beta)$ are satisfied.

$$\begin{cases} \alpha > 2\delta \\ \beta > \alpha \dfrac{5\alpha\delta + 4\delta^2}{2(\alpha - 2\delta)} \end{cases} \tag{32}$$

Where $\delta$ is a known positive constant related to the bound of the disturbance.

### B. MSC current control loop

The tracking errors of the generator d-q current components $(i_{ds}, i_{qs})$ are selected as a sliding surface

$$\begin{cases} s(i_{ds}) = i_{ds}^* - i_{ds} \\ s(i_{qs}) = i_{qs}^* - i_{qs} \end{cases} \tag{33}$$

The dynamics of tracking errors for generator currents, performed from (1) and (33), have the following expressions

$$\begin{cases} \dot{s}(i_{ds}) = \dfrac{di_{ds}^*}{dt} - \dfrac{di_{ds}}{dt} = \left(\dfrac{di_{ds}^*}{dt} + \dfrac{r_s}{L_d}i_{ds} + \dfrac{L_q\omega_e}{L_d}i_{qs} - \dfrac{M_{sQ}\omega_e}{L_d}i_Q + \dfrac{v_{ds}}{L_d}\right) + \xi_d = u_d + \xi_d \\ \dot{s}(i_{qs}) = \dfrac{di_{qs}^*}{dt} - \dfrac{di_{qs}}{dt} = \left(\dfrac{di_{qs}^*}{dt} + \dfrac{r_s}{L_q}i_{qs} + \omega_e i_{ds} - \dfrac{M_{sQ}\omega_e}{L_q}i_Q + \dfrac{v_{qs}}{L_q}\right) + \xi_q = u_q + \xi_q \end{cases} \tag{34}$$

Where $u_d$ and $u_q$ are the new control inputs, $\xi_d$ and $\xi_q$ are disturbances linked to unmodeled dynamics, parametric uncertainties and any potential perturbation.

The d-q components of the control input $(v_{ds}^*, v_{qs}^*)$, are obtained by substituting the SOSMC law (26) into the control inputs of (34), as follows:

$$\begin{cases} v_{ds}^* = L_d\left(-\alpha|s|^{\frac{1}{2}} sign(s) + u_d - \dfrac{r_s}{L_d}i_{ds} - \dfrac{L_q\omega_e}{L_d}i_{qs} + \dfrac{M_{sQ}\omega_e}{L_d}i_Q - i_{ds}^*\right) \\ \dot{u}_d = -\beta \, sign(s) \\ v_{qs}^* = L_q\left(-\alpha|s|^{\frac{1}{2}} sign(s) + u_q - \dfrac{r_s}{L_q}i_{qs} - \omega_e i_{ds} + \dfrac{M_{sQ}\omega_e}{L_q}i_Q - i_{qs}^*\right) \\ \dot{u}_q = -\beta \, sign(s) \end{cases} \tag{35}$$

### C. GSC current control loop

For the second part of the filter, the same steps are used, but the control is implemented on the PNS components of the grid currents.

The d-q positive components of the control input $(v_{di}^{+*}, v_{qi}^{+*})$, are determined from (5), using the SOSMC law (26), such as:

$$\begin{cases} v_{di}^{+*} = L_f\left(-\alpha|s|^{\frac{1}{2}} sign(s) + u_{d1} + \dfrac{r_f}{L_f}i_{dg}^{+} - \omega_g i_{qg}^{+} + \dfrac{1}{L_f}v_{dg}^{+} + i_{dg}^{+*}\right) \\ \dot{u}_{d1} = -\beta\, sign(s) \\ v_{qi}^{+*} = L_f\left(-\alpha|s|^{\frac{1}{2}} sign(s) + u_{q1} + \dfrac{r_f}{L_f}i_{qg}^{+} + \omega_g i_{dg}^{+} + \dfrac{1}{L_f}v_{qg}^{+} + i_{qg}^{+*}\right) \\ \dot{u}_{q1} = -\beta\, sign(s) \end{cases} \qquad (36)$$

Similarly, the *d-q* negative components of the control input $\left(v_{di}^{-*}, v_{qi}^{-*}\right)$, are determined from (6), using the SOSMC law (26), such as:

$$\begin{cases} v_{di}^{-*} = L_f\left(-\alpha|s|^{\frac{1}{2}} sign(s) + u_{d2} + \dfrac{r_f}{L_f}i_{dg}^{-} + \omega_g i_{qg}^{-} + \dfrac{1}{L_f}v_{dg}^{-} + i_{dg}^{-*}\right) \\ \dot{u}_{d2} = -\beta\, sign(s) \\ v_{qi}^{-*} = L_f\left(-\alpha|s|^{\frac{1}{2}} sign(s) + u_{q2} + \dfrac{r_f}{L_f}i_{qg}^{-} - \omega_g i_{dg}^{-} + \dfrac{1}{L_f}v_{qg}^{-} + i_{qg}^{-*}\right) \\ \dot{u}_{q2} = -\beta\, sign(s) \end{cases} \qquad (37)$$

Finally, the *d-q* component of the control input is given by

$$\begin{cases} v_{di}^{*} = v_{di}^{+*} + v_{di}^{-*} \\ v_{qi}^{*} = v_{qi}^{+*} + v_{qi}^{-*} \end{cases} \qquad (38)$$

## VI. SIMULATION RESULTS AND DISCUSSION

A series of simulation scenarios have been performed using MATLAB/Simulink in order to evaluate the effectiveness of the proposed control strategies for the WFSG system under network unbalances against the three control targets defined previously.

The parameter values of the WECS used in these simulations are given in Appendix A. The nominal DC-link voltage is 600 V and the switching frequency is 10 kHz for both MSC and GSC. The wind speed is fixed at 8 m/s throughout the simulations.

### A. Operation under single-phase to ground fault

In this scenario, an unbalance of type B, i.e., single line to ground (1L-G) fault with a 60% dip depth, was applied in phase 'a' at $t = 3$ sec and cleared after $t = 0.15$ sec, as depicted in Fig. 7.
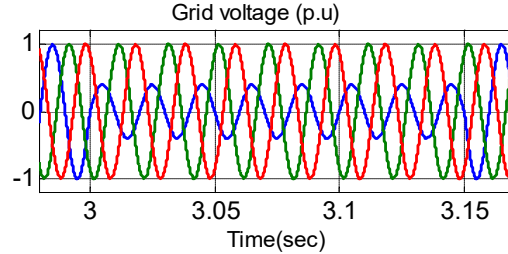


**Fig. 7.** Single-phase unbalanced grid voltages.

The simulation results of the WFSG system with the proposed control applied to both MSC and GSC are shown in Figs. 8-9, 10-11, and 12-13 for Targets (**i**), (**ii**), and (**iii**) respectively. During the simulation, the MSC is controlled to store the surplus energy in the rotor inertia by reducing the real power of the WFSG to zero, while the GSC is controlled to achieve three different control targets.

As shown in Fig. 8(b), when the grid fault occurs, the real power of the WFSG suddenly drops to zero by controlling the electromagnetic power of the WFSG. Subsequently, both the current and electromagnetic torque of the generator decrease to zero. Consequently, the generator speed will increase as a result of the unbalance between the electrical and mechanical torque as illustrated by Figs. 8(a), (b), (c).Then, the excess power will be stored in the inertia of the turbine-generator system. Therefore, the oscillations of the DC-link voltage have been removed. However, as shown in Figs. 8(d), 11(d), and 12(d), these responses show a peak during the appearance and clearance of the fault when the MSC control operation changes from normal to LVRT control.

Moreover, during the grid fault, $i_{qg}$ changes from 0 to 1.2 pu to compensate for the required reactive current; while the real power injected to the grid is reduced to 0 pu due to this large voltage dip, as shown in Figs. 9(f), 11(f), and 13(f). Therefore, the requirement of GCs has been successfully met. The NS components of the d- and q-axis grid currents are shown in Fig. 9(d) and (e), respectively. Note that, these NS currents should be controlled to zero in order to obtain balanced grid currents as shown in Fig. 9(a).
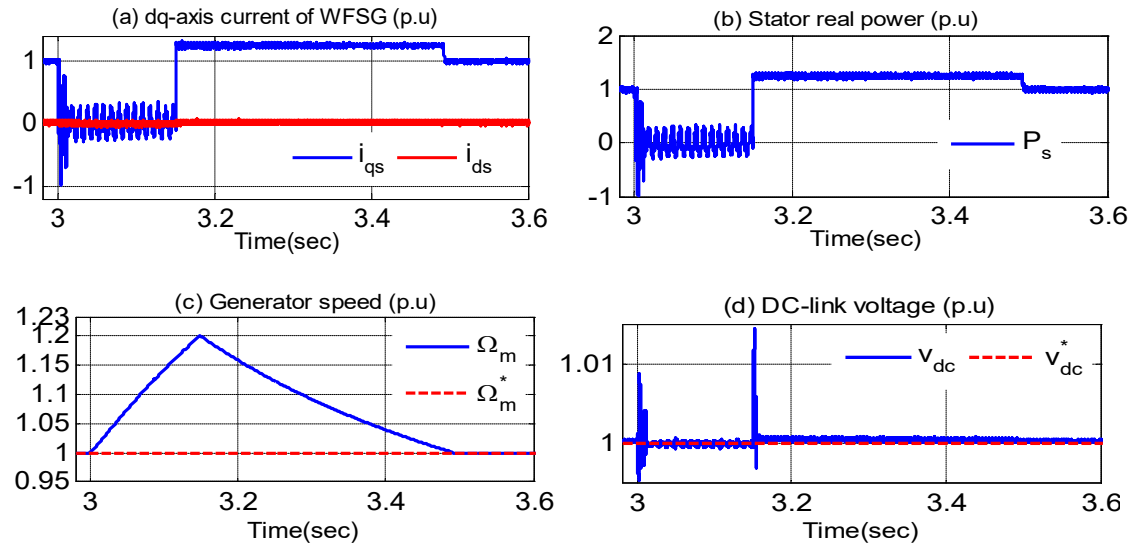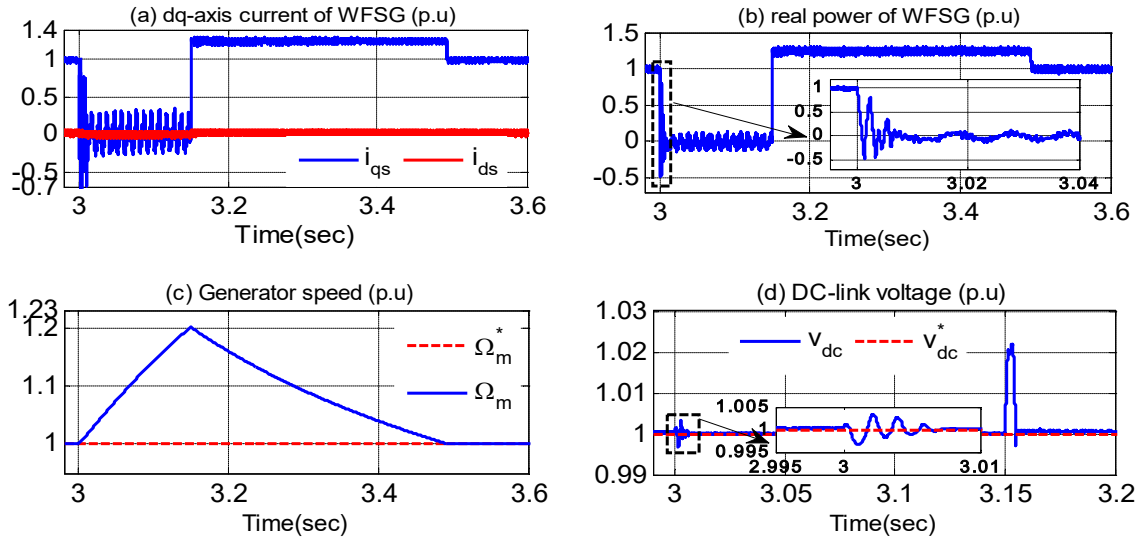


**Fig. 8.** Performance of the MSC under unbalanced sag using the proposed control scheme with Target (**i**). (a) stator *dq*-axis currents (pu), (b) stator real power (pu), (c) generator speed (pu), (d) DC-link voltage (pu).
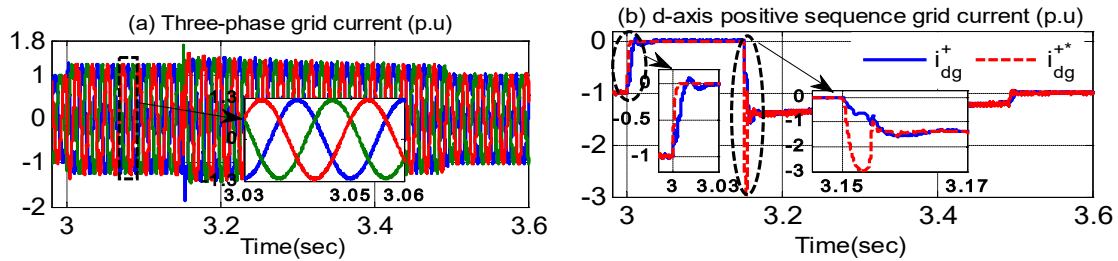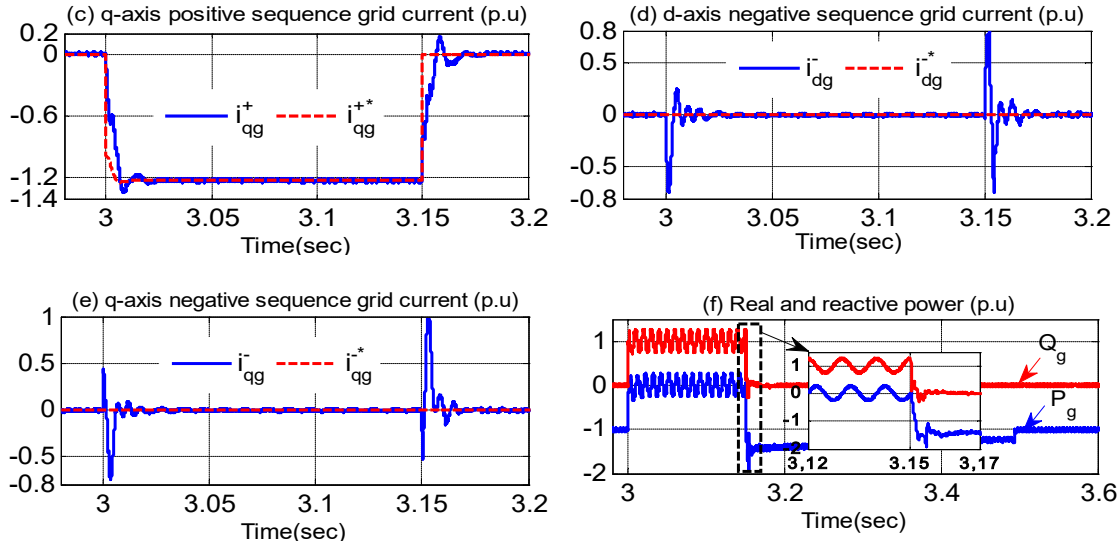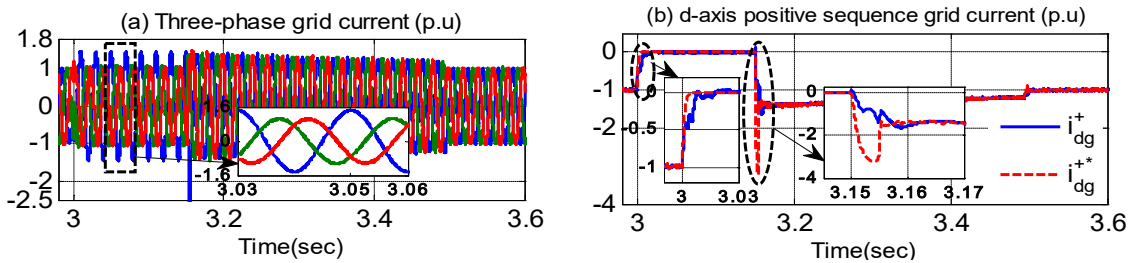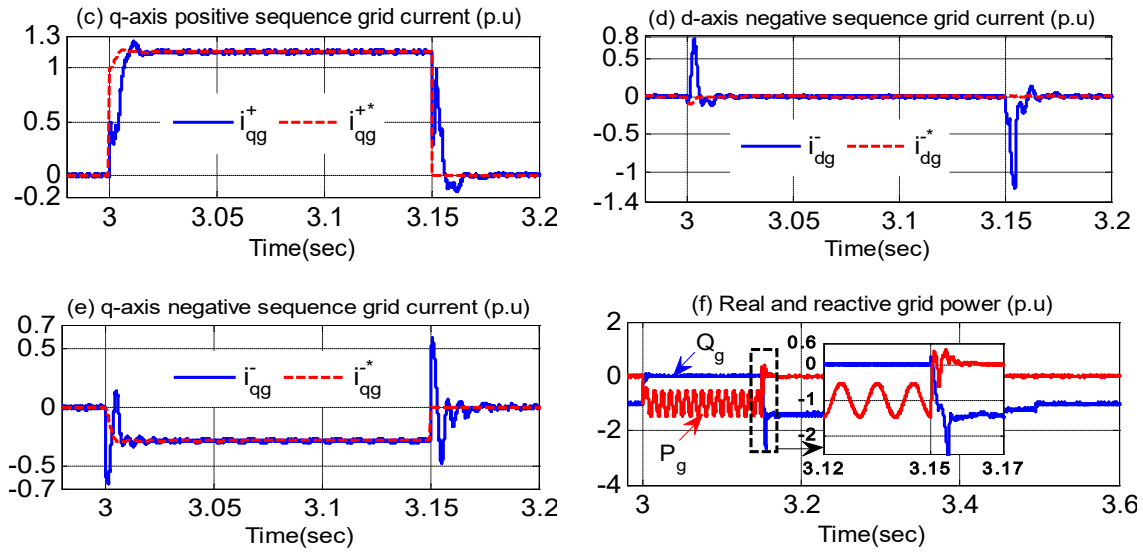
**Fig. 9.** Performance of the GSC under unbalanced sag using the proposed control scheme with Target (**i**). (a) grid phase currents (pu), (b) d-axis positive-sequence grid currents (pu), (c) *q*-axis positive sequence grid currents (pu), (d) *d*-axis negative sequence grid currents (pu), (e) *q*-axis negative-sequence grid currents (pu), (f) real and reactive grid power (pu).
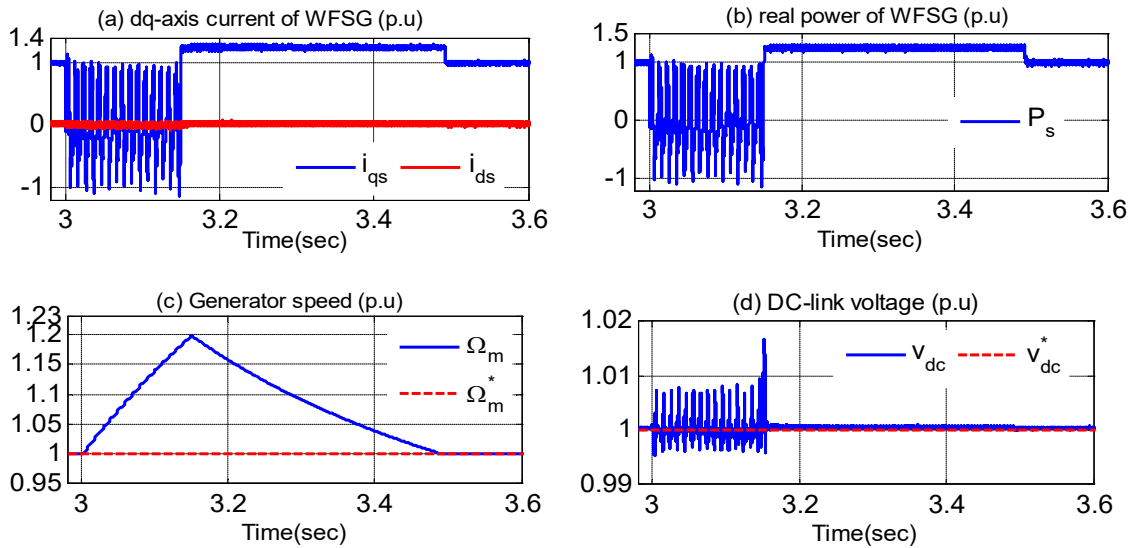


**Fig. 10.** Performance of the MSC under unbalanced sag using the proposed control scheme with Target (**ii**). (a) stator *dq*-axis currents (pu), (b) stator real power (pu), (c) generator speed (pu), (d) DC-link voltage (pu).
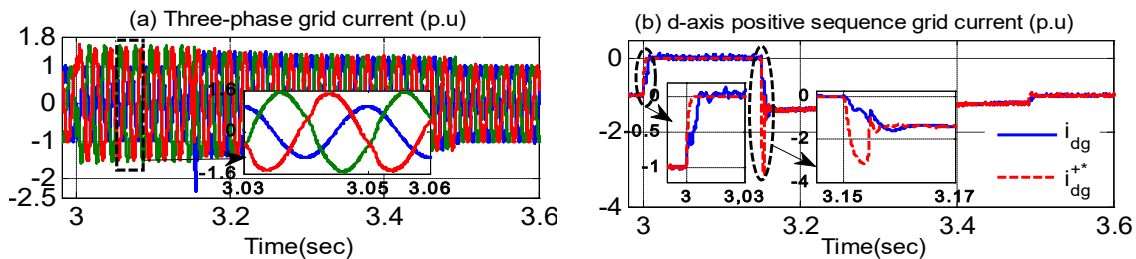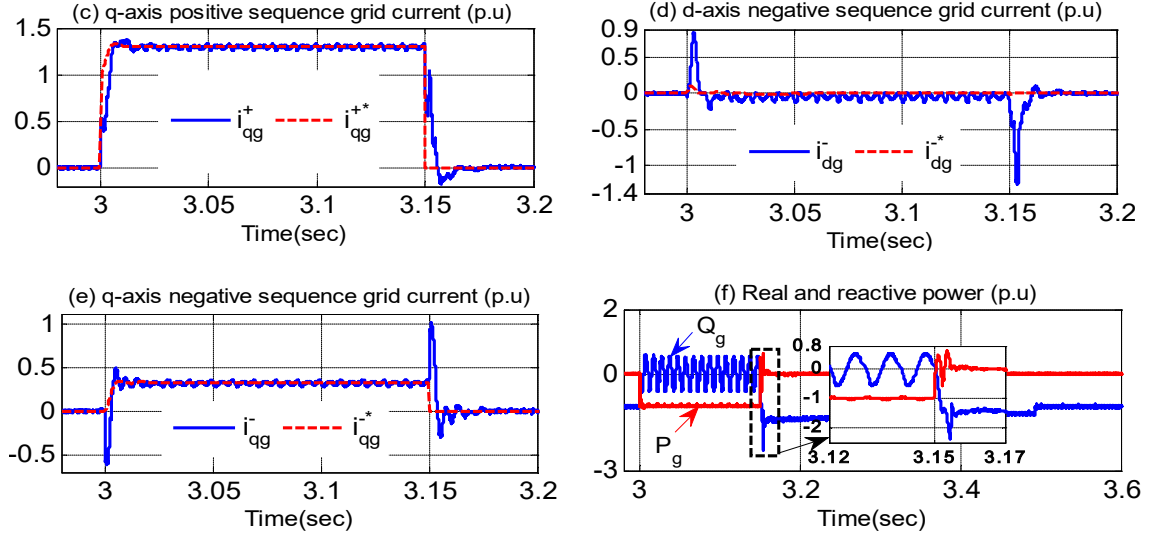


18

**Fig. 11.** Performance of the GSC under unbalanced sag using the proposed control scheme with Target (**ii**). (a) grid phase currents (pu), (b) d-axis positive-sequence grid currents (pu), (c) *q*-axis positive sequence grid currents (pu), (d) *d*-axis negative sequence grid currents (pu), (e) *q*-axis negative-sequence grid currents (pu), (f) real and reactive grid power (pu).



**Fig. 12.** Performance of the MSC under unbalanced sag using the proposed control scheme with Target (**iii**). (a) stator *dq*-axis currents (pu), (b) stator real power (pu), (c) generator speed (pu), (d) DC-link voltage (pu).

**Fig. 13.** Performance of the GSC under unbalanced sag using the proposed control scheme with Target (**iii**). (a) grid phase currents (pu), (b) d-axis positive-sequence grid currents (pu), (c) *q*-axis positive sequence grid currents (pu), (d) *d*-axis negative sequence grid currents (pu), (e) *q*-axis negative-sequence grid currents (pu), (f) real and reactive grid power (pu).

After fault clearance, the MSC returns to normal operation and the energy stored in the inertia is delivered to the grid through the DC-link. The power injected into the grid after the fault is equal to the sum of the captured wind power and the power stored during the fault. Hence, the *q*-axis and *d*-axis currents of the WFSG and GSC reach their limits ($i_{dg} = 11$ A and $i_{qs} = 20$ A) as shown in Figs. 8(a), 9(b). Consequently, the speed of the WFSG starts to decrease, to reach the pre-fault value after all the stored energy has been released and delivered to the grid. As a result, the real power produced by the generator is larger than its previous value (see $P_s$ in Fig. 8(b)). Then, the DC-link voltage injects a real power into the grid more than that generated so that it is restored to the pre-fault value as shown in Figs. 8(d), 9(f).

The three control targets of the GSC are also compared in Table 1. These results demonstrate that, by implementing these controlled targets, the objectives have been fully achieved.

**Table 1.** Comparison of the selectable control targets during network unbalance.

| Control targets (%) | Targets | | |
|---|---|---|---|
| | **(i)** | **(ii)** | **(iii)** |
| Unbalance in $I_g$ | 0.1 | 7.1 | 7.6 |
| Oscillations in $P_g$ | ±9.3 | ±0.3 | ±14.2 |
| Oscillations in $Q_g$ | ±7.2 | ±16.2 | ±0.3 |
| Oscillations in $P_s$ | ±5.5 | ±1.3 | ±7.3 |

When Target (**i**) is adopted, as shown in Fig. 9(d) and (e), the NS of the GSC's current has been successfully eliminated as discussed in Section 3. It was found that only 0.1% of the total current was unbalanced, and the total real and reactive power oscillations produced were ±7.2% and ±9.3% respectively, as shown in Fig. 9(f). When Target (**ii**) is selected, the real power oscillation at the double grid frequency decreased to ±0.3%, which is depicted in Fig. 11(f). However, according to Fig. 11(f) and (a) the oscillations in the reactive power have increased to ±16.2% and as a result, the total unbalanced grid current has increased to 7.1%. In Fig. 13, Target (**iii**) successfully restrains the oscillations in the reactive power injected into the grid (within ±0.3%), as shown in

20

Fig. 13(f). However, the real power oscillations have greatly increased to ±14.2%, which caused the increasing the stator real power oscillations (within ±7.3%) compared to control Target (**ii**) (within ±1.3%). On the other hand, the grid current became unbalanced.

To further demonstrate the effectiveness of the proposed control scheme under grid voltage unbalance, the harmonic spectra of the outputs: grid current, real power and reactive power for the three targets are analysed and compared in Fig. 14. These results show that the Total Harmonic Distortion (THD) of the grid current for the three targets is under the 5% limit as required by IEEE 519 standards. Therefore, the GC requirement has been successfully fulfilled. Moreover, the grid real and reactive powers contain significant oscillations at twice the grid frequency (100 Hz), that is, a second order harmonic according to the control target chosen.



(a) Target (**i**)          (b) Target (**ii**)          (c) Target (**iii**)
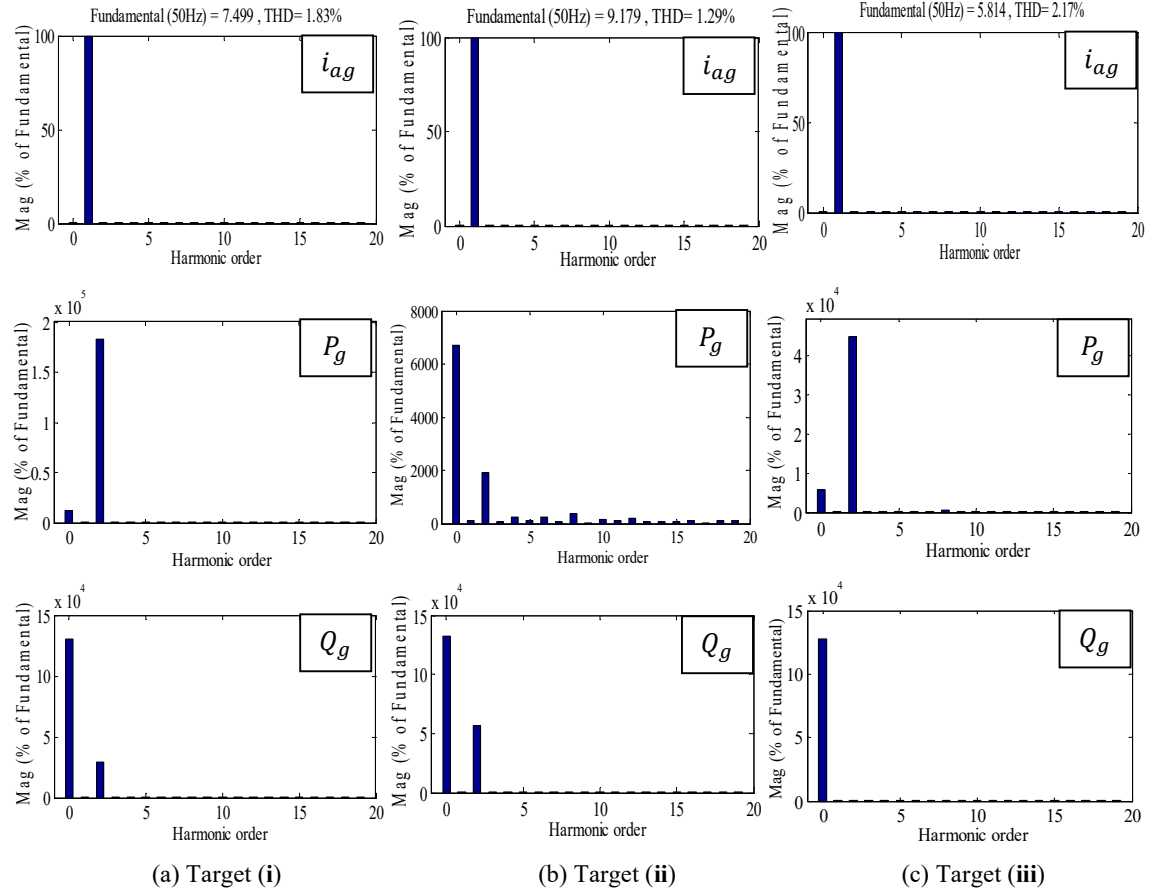
**Fig. 14.** Harmonic spectra with the proposed control strategy under 60% unbalanced grid voltage between 3– 3.15s.

From the previous analysis, it can be concluded that the proposed control strategy was able to reduce the grid real and reactive power oscillations and remove the output current unbalance. Hence, the dynamic performance of the WFSG-driven wind turbine under an unbalanced condition has been significantly enhanced. The proposed controller achieved good steady-state performance, good harmonic mitigation and satisfactory dynamic response for the overall WFSG system during fault conditions. Consequently, the FRT capability of the WFSG wind turbine system to stay connected to the grid network, during grid faults has been greatly improved.

**B.   Comparative study under three-phase to ground fault**

In this scenario, the performance of the SOSMC controller is investigated under three-phase to ground fault, it has been compared with the PI controller. The fault was simulated as a voltage drop of 60% of its nominal value for a period of 0.15 sec between t = 3 sec and t = 3.15 sec (see Fig. 15). The simulation results are presented in Fig. 16. Target (i) is selected for the following test.
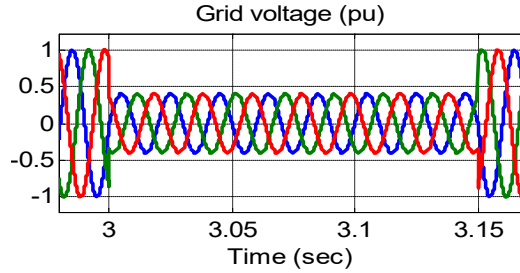


**Fig. 15.** Grid voltage during three-phase to ground fault.

Through these results, it can be seen that the grid currents ($I_{dg}^+$ and ($I_{qg}^+$) corresponding to the real and reactive power with the SOSMC controller have been kept to their desired values during normal and LVRT operation with a lower steady-state error of 1.8 % in comparison to the 2.95 % for PI controller. Moreover, during the fault, the positive component of q-axis current of the GSC reached its limit while the NS components are driven to 0. Also, during a transient state (at t=3sec and t=3.15sec), it is shown that there are lower fluctuations in the DC-link voltage and grid currents waveforms than in the case of the PI controller. Thus, it can be concluded that the SOSMC provides a faster transient response and a smoother steady-state response with less fluctuations under fault conditions. A detailed comparison of the performance of both controllers is presented in Table 2.

(e) DC-link voltage (p.u)
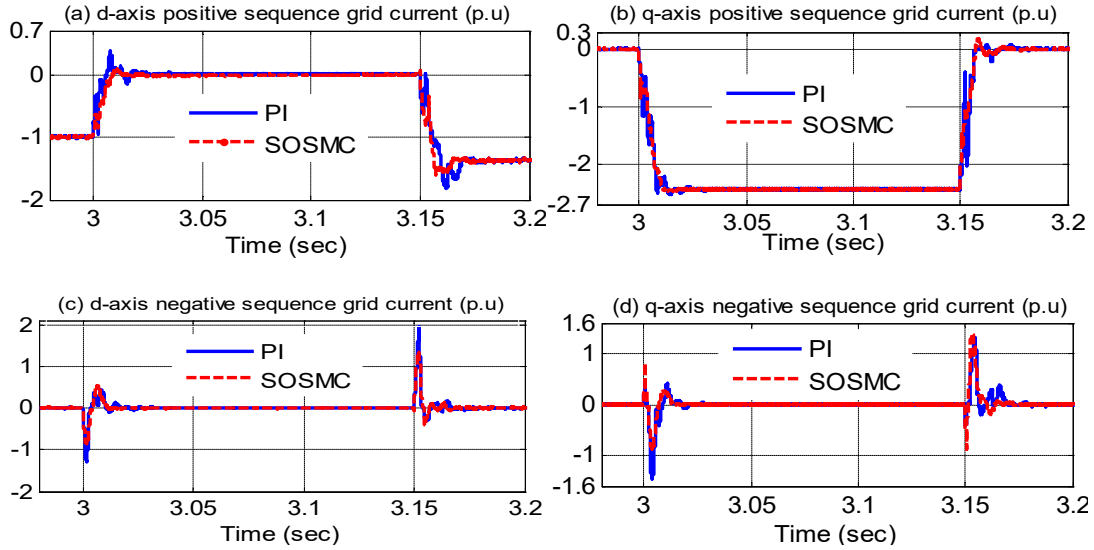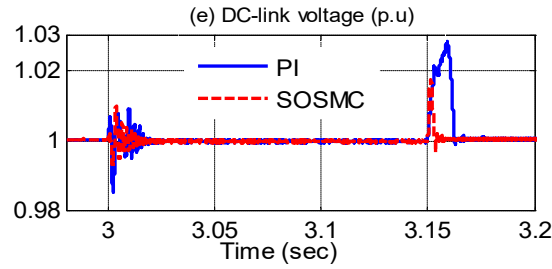
**Fig. 16.** Performance comparison between the proposed controller and PI controller for the three-phase to ground fault. (a) d-axis positive-sequence grid currents (pu), (b) q-axis positive sequence grid currents (pu), (c) d-axis negative sequence grid currents (pu), (d) $q$-axis negative-sequence grid currents (pu), (e) DC-link voltage (pu).

**Table 2.** Comparison between both controller's in terms of their performances at the fault's start time.

| Type of controller | | | | | | | |
|---|---|---|---|---|---|---|---|
| PI controller | | | | SOSMC controller | | | |
| $M_p$ | $E_{ss}$ | $t_r$ | $t_s$ | $M_p$ | $E_{ss}$ | $t_r$ | $t_s$ |
| 0.35 | 0.1 | 0.026 | 0.1 | 0.2 | 0.01 | 0.015 | 0.024 |

A simulation with more severe voltage dips has been performed to assess the performance of the control by focusing on the current of the GSC as presented in Fig. 17. A three-phase to ground fault was applied to the Point of Common Coupling (PCC) for the duration of 0.15 s (between 3 and 3.15 s) and target (i) is selected for the following test. From the simulation results, it can be seen that immediately following the grid voltage dip, the input line current suddenly increases according to the percentage of grid voltage drop and then the system regains its stability. For instance, it can be observed that there is a sudden increase in the current of the GSC up to 2.45 pu when the network voltage suddenly drops to 40% of its normal value. However, the reactive power reference can be reduced to ensure a safe limit for overcurrent. The grid voltages and currents of the GSC at different severity of the voltage dips are listed in Table 3.



23

(E)
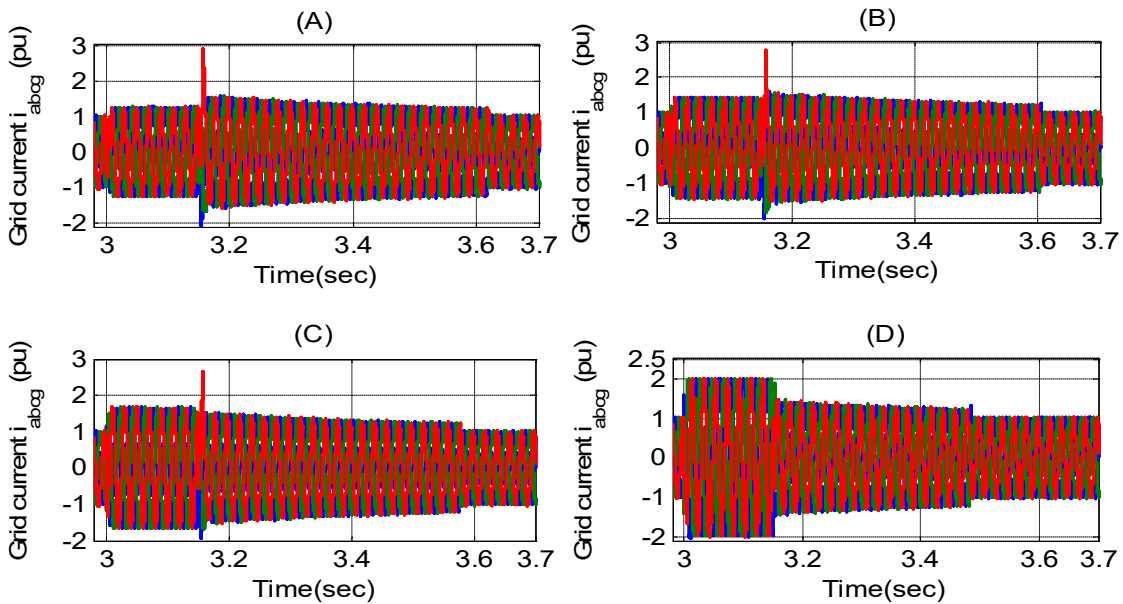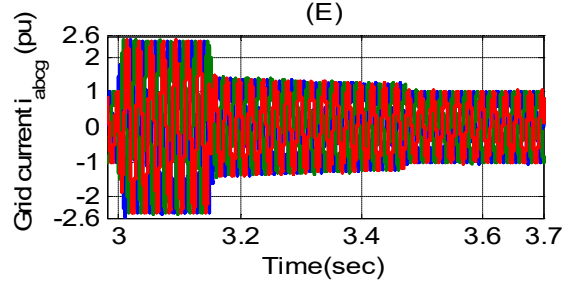
Fig. 17. Transient state response of the system with the proposed control under a three-phase to ground fault.

(A) Grid voltage drops to 80% of its nominal value,

(B) Grid voltage drops to 70% of its nominal value,

(C) Grid voltage drops to 60% of its nominal value,

(D) Grid voltage drops to 50% of its nominal value,

(E) Grid voltage drops to 40% of its nominal value,

Table 3. Assessment parameters of grid-connected VSC system with varying grid voltage.

| Voltage dip severity (%) | $v_{pccd}$ (pu) | $i_{d,ref}$ (pu) |
|---|---|---|
| 100% (Normal grid) | 1 | 1 |
| 80% | 0.8 | 1.22 |
| 70% | 0.7 | 1.4 |
| 60% | 0.6 | 1.64 |
| 50% | 0.5 | 1.95 |
| 40% | 0.4 | 2.45 |

C. **Comparative study under two-phase to ground fault and two-phase short-circuit fault**

In this scenario, the performance of the SOSMC controller was tested for the most severe types of the voltage sag, such as type C (see Fig. 18(a)) and type E (see Fig. 18(b)), and is compared with a PI controller and the results have been presented in Fig. 19 and Fig. 20 respectively. The selected type E voltage sag is a two-phase to ground fault, with the grid voltage drop to 60% of its nominal value, while a two-phase short-circuit fault (BC-phase voltage drop of 20% with the 10-degree phase shift) for the type C voltage sag. Target (**ii**) is selected for the following test.



(a)



(b)
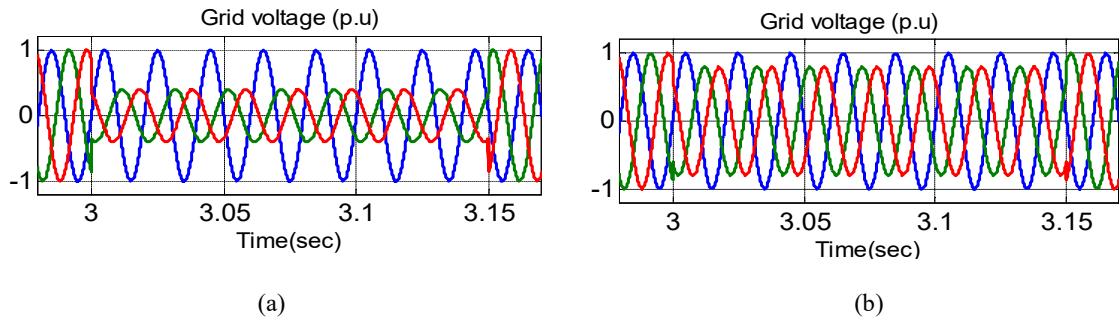
Fig. 18. Three-phase grid voltages: (a) voltage sags Type C, (b) voltage sags Type E.

From these results, it can be observed that the SOSMC controller's transient responses have lower overshoot and smaller steady-state error as compared to the PI controller. Furthermore, the proposed controller leads to less fluctuations during the fault and exhibits a faster dynamic response at the fault clearance time as compared to the PI controller.

Finally, it is worth noting that the tuning of PI controller gains is a delicate task given the complexity and the inherent nonlinearity of the system's dynamics. A change in the reference signal would require re-tuning of the PI parameters whereas the only requirement in the SOSMC controller is to satisfy the conditions (32).
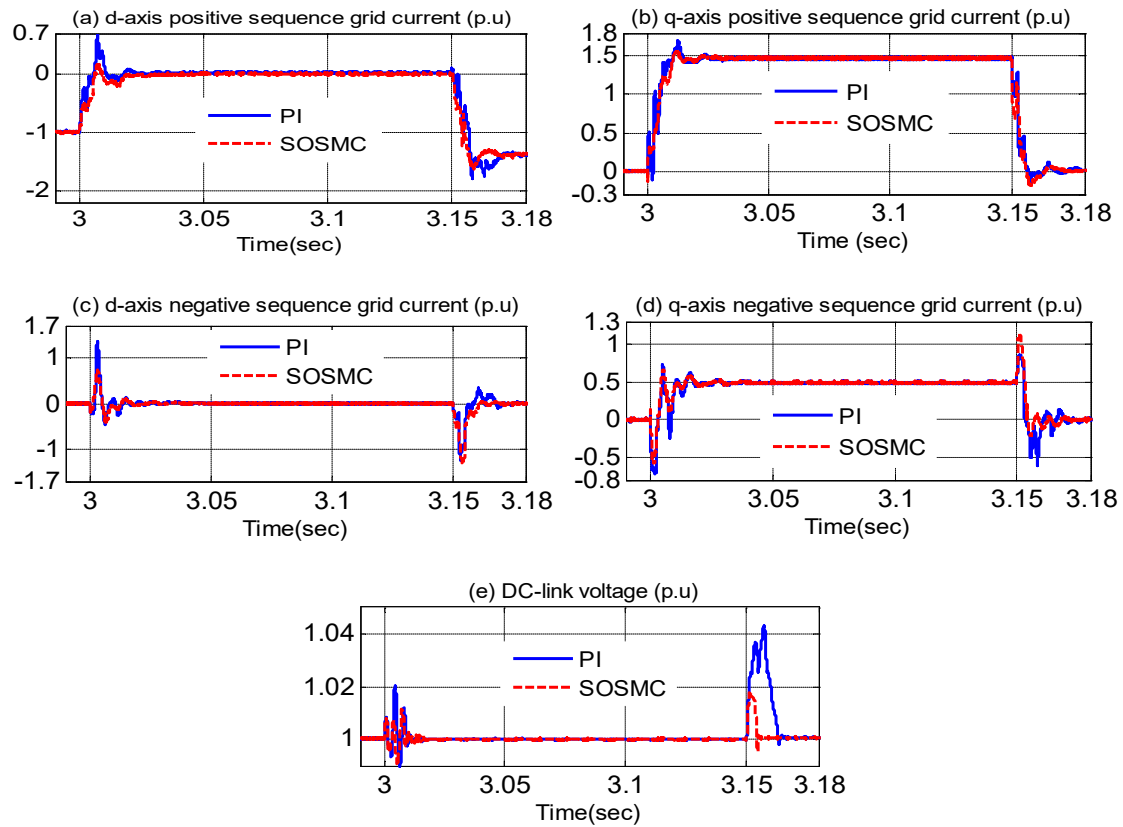


**Fig. 19.** Performance comparison between the proposed controller and PI controller for the C type voltage sag. (a) d-axis positive-sequence grid currents (pu), (b) q-axis positive sequence grid currents (pu), (c) d-axis negative sequence grid currents (pu), (d) $q$-axis negative-sequence grid currents (pu), (e) DC-link voltage (pu).
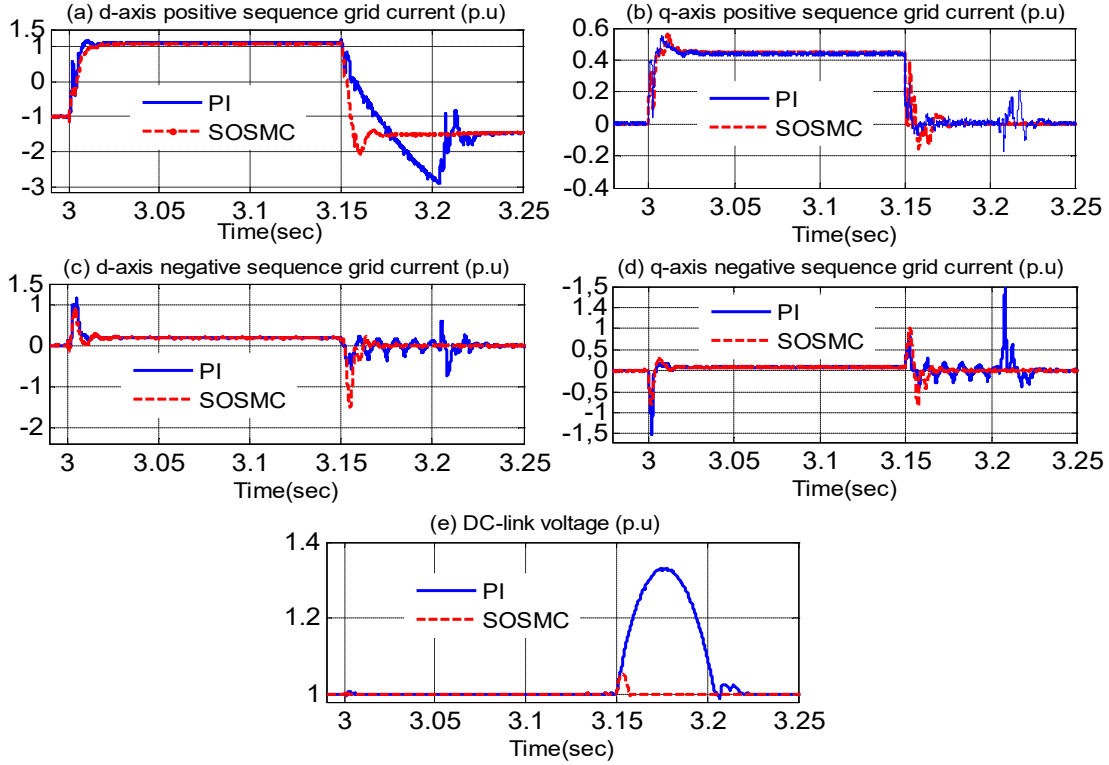
**Fig. 20.** Performance comparison between the proposed controller and PI controller for the E type voltage sag. (a) d-axis positive-sequence grid currents (pu), (b) q-axis positive sequence grid currents (pu), (c) d-axis negative sequence grid currents (pu), (d) *q*-axis negative-sequence grid currents (pu), (e) DC-link voltage (pu).

Table 4 highlights these low voltage effects of grid faults and the various techniques used to mitigate them.

**Table 4** Performance comparison with previous strategies

| Control strategies | Effects of grid faults | | | | | | Effective for fault type | |
|---|---|---|---|---|---|---|---|---|
| | high current peak value | high DC-link peak value | Oscillation of DC-link voltage | Oscillation of real power | Oscillation of reactive power | Reactive power supply | Balanced | Unbalanced |
| [4] | √ | √ | – | – | – | √ | yes | no |
| [35] | √ | √ | – | – | – | – | yes | yes |
| [42] | – | √ | √ | √ | √ | – | yes | yes |
| [46] | √ | √ | – | – | – | √ | yes | yes |
| [47] | √ | √ | √ | √ | √ | – | yes | yes |
| proposal | √ | √ | √ | √ | √ | √ | yes | yes |

## VII. CONCLUSION

The paper proposed an effective control scheme for a wind turbine-driven by a WFSG operating under unbalanced grid voltage conditions and subjected to the E.ON-GC for LVRT requirements. In the suggested control scheme, the MSC is controlled to store excess energy in the inertia of the turbine-generator system, when a fault occurs, and this energy can be dissipated in the crowbar circuit when the generator speed exceeds its operating limit, while the GSC is controlled to follow the alternative targets by using a DDSRF *d-q* current controller. A robust controller based on ST algorithm SOSMC has been designed for both the MSC and GSC current regulation.

From the simulation results the following conclusions are drawn:

1)  The DC-link voltage ripples have been reduced by the GSC controller during the unbalanced grid fault.

2)  The PNS currents are controlled during an unbalanced grid fault and the requirements of the three control targets have been fully achieved. When achieving Target (**i**), the unbalanced current is quickly mitigated to 0.1%, while for Target (**ii**) and (**iii**), the oscillations in the grid real and reactive powers are successfully reduced to ±0.3%.

3)  When a fault occurs in the grid, the GSC can provide maximum reactive power support to the grid, while maintaining its current within its rated value.

4)  A superior performance, with improved transient and steady-state response characteristics, was achieved by the proposed controller as compared to the conventional PI controller during unbalanced grid voltage conditions.

For future works, the authors suggest testing the proposed control strategies on the megawatt range WFSG-based wind turbine model. The models and control strategies proposed in this paper could also be extended to the transmission network connected wind farm to evaluate the impact of severe voltage dips against the above LFRT grid code.

**REFERENCES**

[1] Khajeh A. and Ghazi R., Control of DFIG Wind turbines based on indirect matrix converters in short circuit mode to improve the LVRT capability, Advances in Power Electronics, vol. 2013, Article ID 157431.

[2] Global Wind Energy Council (GWEC). Global Wind Report 2018. Available online: http://www.gwec.net/(accessed on 13 August 2018).

[3] Benbouzid M.H., Beltran B., Amirat Y., Yao G., Han J. and Mangel H., Second-order sliding mode control for DFIG-based wind turbines fault ride-through capability enhancement. *ISA Transactions* 2014; 53(3): 827–833.

[4] Yaramasu V., B Wu B., Alepuz S. and Kouro S., Predictive control for low voltage ride-through Enhancement of three-level boost and NPC converter based PMSG wind turbine. *IEEE Trans. Ind. Electronics*, 2014; 61(12) : 6832–6843.

[5] Fang Y., LihuiY.and Xikui M., An advanced control strategy of PV system for low-voltage ride through capability enhancement, *Solar Energy* 2014; 109: 24–35.

[6] Hae G. J. and Kyo B. L. A control scheme to fulfill the grid-code under various fault conditions in the grid-connected wind turbines. *J. of Electrical Engineering*,2014; 96(2): 199–210.

[7] Boëda, D., Teninge, A., Roye, D., Bacha, S., and Belhomme, R. Contribution of wind farms to frequency control and network stability, Proceedings of European Wind Energy Conference (EWEC), Milano, Italia, 2007.

[8] Teninge A., Roye D., and Bacha S. Reactive power control for variable speed wind turbines to low voltage ride through grid code compliance, XIX IEEE International Conference on Electrical Machines (ICEM), 2010.

[9] Rini Ann Jerin Amalorpavara., Palanisamy Kaliannan and Umashankar Subramaniam. Improved fault ride through capability of DFIG based wind turbines using synchronous reference frame control based dynamic Voltage Restorer. *ISA Transactions* 2017; 70: 465–474.

[10] E.ON Netz GmbH. Grid code-high and extra high voltage, Germany, April 2006. 783 Available at: <http://www.thewindpower.net>.

[11] Jingya D., Dewei X., Bin W. and Zargari N.R. Unified DC-link current control for low voltage ride-through in current source converter-based wind energy conversion systems, IEEE Trans. Power Electronics, 2011; 21(1): 288–297.

[12] Li, B.; Liu, J.; Wang, X.; Zhao, L. Fault Studies and Distance Protection of Transmission Lines Connected to DFIG-Based Wind Farms. *Appl. Sci.* **2018**, *8*, 562.

[13] Topal M. E. and Ergene L. T. Designing a wind turbine with permanent magnet synchronous machine, Istanbul University J. of Electrical and Electronic Eng. (IU-JEEE) 2011; 11(1): 1311–7.

[14] Alepuz S, Calle A., Monge S.B., Kouro S. and Wu B. Use of stored energy in PMSG rotor inertia for low-voltage ride-through in back-to-back NPC converter-based wind power systems, *IEEE Trans. Ind. Electronics*, 2013; 60: 1787–96.

[15] Heng N., Yipeng S., Peng Z. and Yikang H. Improved Direct Power Control of a wind turbine driven doubly fed induction generator during transient grid voltage unbalance, *IEEE Trans. Energy Conversion*, 2011; 26: 976- 986.

[16] Zhou Y., Bauer P., Ferreira J. A. and Pierik J. Operation of grid connected DFIG under unbalanced grid voltage condition, *IEEE Trans. Energy Conversion*, 2009; 24(1): 240–246.

[17] Tsili M. and Papathanassiou S. A review of grid code technical requirements for wind farms, *IET Renew. Power Generation*, 2009; 3(3): 308–332.

[18] G. Pannell, B. Zahawi, D. J. Atkinson, and P. Missailidis, "Evaluation of the performance of a DC-link brake chopper as a DFIG low voltage fault ride through device," *IEEE Trans. Energy Convers*., 2013; 28(3): 535-542.

[19] A. Gencer, Analysis and Control of Fault Ride Through Capability Improvement PMSG Based on WECS Using Active Crowbar System During Different Fault Conditions. *Elektronika ir Elektrotechnika* 2018; 24: 64-69.

[20] Mendes, V.F., Matos, F.F.; Liu, S.Y., Cupertino, A.F.; Pereira, H.A. and de Sousa, C.V. Low voltage ride-through capability solutions for permanent magnet synchronous wind generators, *Energies*, 2016; 9:59.

[21] Nguyen TH, Lee DC. Advanced fault ride-through technique for PMSG wind turbine systems using line-side converter as STATCOM. IEEE T Ind Elec 2013; 7: 2842-2850.

[22] Sivasankar G, Suresh Kumar V. Supercapacitor energy storage based-UPQC to enhance ride-through capability of wind turbine generators. Turk J ElecEng& Comp Sci 2015; 23: 1867-1881.

[23] Goweily, K., El Moursi, M., Abdel-Rahman, M.,Badr, M.A.L., Voltage booster scheme for enhancing the fault ride-through of wind turbines. *IET Power Electron*. 2015; 8: 1853–1863.

[24] Causebrook, A.; Atkinson, D.J.; Jack, A.G., Fault ride-through of large wind farms using series dynamic braking resistors. *IEEE Trans. Power Syst*. 2007; 22: 966–975.

[25] Tongzhou, J.; Xiongfeng, H.; Xianyun, L.; Kun, L.; Mei, Z. Performance analysis and research on LVRT of PMSG wind power system with SDBR. In Proceedings of the 33rd Chinese Control Conference, Nanjing, China, 28–30 July 2014.

[26] Wu, Z., Dou, X., Chu, J. and Hu, M. Operation and control of a direct-driven PMSG-based wind turbine system with an auxiliary parallel grid-side converter. Energies. 2013; 6: 3405–3421.

[27] Huang, H., Mao, C., Lu, J. and Wang, D., Electronic power transformer control strategy in wind energy conversion systems for low voltage ride-through capability enhancement of directly driven wind turbines with permanent magnet synchronous generators (D-PMSGs), Energies 2014; 7: 7330–7347.

[28] Yehia DM, Mansour DA, Yuan W. Fault ride-through enhancement of PMSG wind turbines with DC microgrids using resistive-type SFCL. IEEE Trans Appl Superconductivity. 2018;28(4):1-5.

[29] Chen L, He H, Chen H, et al. Study of a modified flux-coupling-type SFCL for efficient fault ride-through in a PMSG wind turbine under different types of faults. Can J Elect Comput Eng. 2017;40(3):189-200.

[30] Huang C, Xiao XY, Zheng Z, Wang Y. Cooperative control of SFCL and SMES for protecting PMSG-based WTGs under grid faults. IEEE Trans Appl Superconductivity. 2019;29(2):1-6.

[31] Firouzi M. A modified capacitive bridge-type fault current limiter (CBFCL) for LVRT performance enhancement of wind power plants. Int Trans Electr Energy Syst. 2018;28(3):e2505.

[32] Hossain ME. Performance analysis of diode-bridge-type non-superconducting fault current limiter in improving transient stability of DFIG based variable speed wind generator. Electr Pow Syst Res. 2017;143:782-793.

[33] Firouzi M, Gharehpetian GB. Improving fault ride-through capability of fixed-speed wind turbine by using bridge-type fault current limiter. IEEE Trans Energy Convers. 2013;28(2):361-369.

[34] Firouzi M, Nasiri M, Benbouzid M, Gharehpetian GB. Application of multi-step bridge-type fault current limiter for fault ride-through capability enhancement of permanent magnet synchronous generator-based wind turbines. Int Trans Electr Energy Syst. 2020;30(11):e12611.

[35] Andres E. Leon, Marcelo F. Farias, Pedro E. Battaiotto, Jorge A. Solsona, and María Inés Valla, Control strategy of a DVR to improve stability in wind farms using squirrel-cage induction generators, IEEE Transactions on Power Systems, 2011; 26(3): 1609-1617.

[36] Zhang, S., Tseng, K. S., Choi, S., Nguyen, T.D. and Yao D., Advanced control of series voltage compensation to enhance wind turbine ride-through, IEEE Transactions on Power Electronics, 2012; 27( 2): 763–772.

[37] Rini Ann Jerin Amalorpavaraj, Palanisamy Kaliannan, Sanjeevikumar Padmanaban Umashankar Subramaniam and Vigna K. Ramachandaramurth. Improved fault ride through capability in DFIG based wind turbines using dynamic voltage restorer with combined feed-forward and feed-back control, IEEE Access, 2017; 5: 20494-20503.

[38] Hong-Seok S. and Kwanghee N. Dual current control scheme for PWM converter under unbalanced input voltage conditions, IEEE Trans. Ind. Electronics, 1999; 46: 953-959.

[39] Xu L. Coordinated control of DFIG's rotor and grid side converters during network unbalance, IEEE Trans. Power Electronics, 2008; 23(3): 1041–1049.

[40] Wang M, Shi YY, Qi MY, Shen MH. A three-vector-based direct power control strategy for three-phase voltage source PWM converters. Int J Circuit Theory Appl. 2017; 45(8):1151-1168.

[41] Van-Tung Phan, Thillainathan Logenthiran, Wai Lok Woo, Dave Atkinson, Volker Pickert. Analysis and compensation of voltage unbalance of a DFIG using predictive rotor current control, Int. J. Electrical Power & Energy Systems, 2016; 75: 8–18.

[42] Chenwen C., Peng C., Heng N., Dan S. Model predictive stator current control of doubly fed induction generator during network unbalance. IET Power Electronics, 2018; 11(1): 120-128.

[43] Reyes M., Rodriguez P., Vazquez S, Luna A, and Carrasco. J.M. Enhanced decoupled double synchronous reference frame current controller for unbalanced grid-voltage conditions, IEEE Trans. Power Electronics, 2011; 27(9): 3934–3943.

[44] Zhen L, Siu-Chung W, Chi K. T, Xiangdong L. Controller saturation nonlinearity in doubly fed induction generator based wind turbines under unbalanced grid conditions. Int J Circuit Theory Appl. 2016; 44(8): 1602-1619.

[45] Liserre M., Teodorescu R. and Blaabjerg F. Multiple harmonics control for three-phase grid converter systems with the use of PI-RES current controller in a rotating frame, IEEE Trans. Power Electronics, 2006; 21(3): 836-841.

[46] Etxeberria-Otadui I., Viscarret U., Caballero M., Rufer A. and S. Bacha S., New optimized PWM VSC control structures and strategies under unbalanced voltage transients, IEEE Trans. Ind. Electronics, 2007; 54(5): 2902–2914.

[47] Hu J., He Y., Xu L. and Williams B.W., Improved control of DFIG systems during network unbalance using PI–R current regulators, *IEEE Trans. Indus Electronics*, 2009; 56(2): 439-451.

[48] Jun Y., Xiyin C., Liao Yong L., Hui L., Song H. A grid connection control strategy to suppress negative-sequence and harmonic currents for permanent magnet direct-driven wind power generation system, *Power System Technology*, 2011; 35(7): 29- 35.

[49] Busada C. A. et al., Current controller based on reduced order generalized integrators for distributed generation systems. *IEEE Trans. Ind. Electron*, 2012, 59(7): 2898-2909.

[50] Peng. C, Heng. N. Collaborative control of DFIG system during network unbalance using reduced-order generalized integrators. *IEEE Trans. Energy Conversion*, 2015, 30(2): 453-464.

[51] Zhao Xin, Jin Xinmin, Zhou Fei, LI Geliang, Unbalanced control of grid-connected inverters based on proportional integral reduced-order resonant controllers[J]. Proceedings of the CSEE, 2013, 33(19):84-92.

[52] Dong, Shuhui, Yonggang Li, Aimeng Wang, and Wenyuan Xi. "Control of PMSG wind turbines based on reduced order resonant controllers under unbalanced grid voltage conditions", 2015 IEEE 11th International Conference on Power Electronics and Drive Systems, 2015.

[53] Tahir K., Belfedal C., Allaoui T., and M. Doumi M. Proposal of a new hybrid control strategy for dynamic performance improvement of wound field synchronous generator-based wind turbines, *J. of Renewable and Sustainable Energy.* 2015; 7(4): 043113.

[54] Gencer, Altan. "Analysis and Control of Fault Ride-Through Capability Improvement for Wind Turbine Based on a Permanent Magnet Synchronous Generator Using an Interval Type-2 Fuzzy Logic System." *Energies.* 2019; 12(12): 2289.

[55] Xiong, Linyun, Penghan Li, and Jie Wang. "High-order sliding mode control of DFIG under unbalanced grid voltage conditions." *International Journal of Electrical Power & Energy Systems* 2020; 117: 105608.

[56] Meng W, Haoran W, Yanyan S, Minghui S, Jian S. A modified sliding-mode controller-based mode predictive control strategy for three-phase. Int J Circuit Theory Appl. 2020; 48(10): 1564-1582.

[57] Barakat A., Tnani S., Champenois G. and Mouni E. Analysis of synchronous machine modeling for simulation and industrial applications, *Simulation Modelling Practice and Theory*, 2010; 18(9): 1382–1396.

[58] Teninge, A., C. Jecu, D. Roye, S. Bacha, J. Duval, and R. Belhomme. "Contribution to frequency control through wind turbine inertial energy storage", *IET Renewable Power Generation*, 2009; 3(3): 358–370.

[59] Yao, Jun, Te Zhou, Weihao Hu, Zhe Chen, Qiping Shen, and Mengting Yu. "Enhanced Control for a Direct-driven Permanent Synchronous Generator Wind-power Generation System with Flywheel Energy Storage Unit Under Unbalanced Grid Fault", *Electric Power Components and Systems*, 2015; 43(8): 982-994.

[60] Rioual P., Pouliquen H., and Louis J., Regulation of a PWM rectifier in the unbalanced network state using a generalized model, *IEEE Trans. Power Electronics*, 1996; 11(3): 495–502.

[61] Teodorescu R, Liserre M, Rodriguez P. Grid converters for photovoltaic and wind power systems. Wiley-IEEE Press, New York, 2011.

[62] Rodríguez P., Luna A., Muñoz-Aguilar R., Etxeberria-Otadui I., Teodorescu R. and Blaabjerg F. A stationary reference frame grid synchronization system for three-phase grid-connected power converters under adverse grid conditions. *IEEE Trans. Power Electronics* 2012; 27(1): 99–112.

[63] Levant A. Sliding order and sliding accuracy in sliding mode control. *Int J Control* 1993;58(6):1247 –63.

[64] Moreno JA, Osorio M. A Lyapunov approach to a second-order sliding mode controllers and observers. Proc. 47th IEEE Conf. Decision and Control, Mexico. 2008. p. 2856–61.

**APPENDICES**

**Appendix A:** Parameters used in the simulation models

| Variable | Description | Value |
|---|---|---|
| **Wind Turbine Parameters** | | |
| $P_t$ | Rated power of the turbine (kW) | 10 |
| $\rho$ | Density area (kg.m$^{-2}$) | 1.225 |
| $R$ | Radius of the turbine (m) | 3 |
| | Number of blades | 3 |
| $G$ | Gear ratio | 5.4 |
| $f$ | Viscous friction coefficient (N.m.s$^{-1}$) | 0.017 |
| **Wound Field Synchronous Generator Parameters** | | |
| $S_n$ | Rated power of the generator (kVA) | 7.5 |
| $r_s$ | Stator resistance ($\Omega$) | 1.19 |
| $r_f$ | Rotor resistance ($\Omega$) | 3.01 |
| $U_{rms}$ | Phase to phase rated voltage (V) | 400 |
| $X_d$ | Direct synchronous reactance (p.u) | 1.4 |
| $X_q$ | Transverse synchronous reactance (p.u) | 0.7 |
| $T_{d0}''$ | Open circuit transient time constant (ms) | 522 |
| $X_d'$ | Direct transient synchronous reactance (p.u) | 0.099 |
| $X_d''$ | Direct sub-transient synchronous reactance (p.u) | 0.049 |
| $T_d'$ | Direct transient time constant (p.u) | 40 |
| $T_d''$ | Direct sub-transient time constant (ms) | 3.7 |
| $T_a$ | Armature time constant (ms) | 6 |
| **Grid Parameters** | | |
| $v_{dc}$ | DC-Link voltage (V) | 600 |
| $C$ | DC capacitance ($\mu$F) | 1500 |
| $V_{rms}$ | Effective voltage (V) | 220 |
| $f_s$ | Frequency (Hz) | 50 |
| $R_f$ | Leakage résistance ($\Omega$) | 1 |
| $L_f$ | The leakage inductance (mH) | 12 |